Geoscience Laser Altimeter System (GLAS)

Algorithm Theoretical Basis Document
Version 2.1

PRECISION ORBIT DETERMINATION (POD)

Prepared by:

H. J. Rim
B. E. Schutz
Center for Space Research
The University of Texas at Austin

February 2001

TABLE OF CONTENTS

1.0   INTRODUCTION

1.1   Background

The EOS ICESat mission is scheduled for launch on July 2001. Three major science objectives of this mission are: (1) to measure long-term changes in the volumes (and mass) of the Greenland and Antarctic ice sheets with sufficient accuracy to assess their impact on global sea level, and to measure seasonal and interannual variability of the surface elevation, (2) to make topographic measurements of the Earth's land surface to provide ground control points for topographic maps and digital elevation models, and to detect topographic change, and (3) to measure the vertical structure and magnitude of cloud and aerosol parameters that are important for the radiative balance of the Earth-atmosphere system, and directly measure the height of atmospheric transition layers. The spacecraft features the Geoscience Laser Altimeter System (GLAS), which will measure a laser pulse round-trip time of flight, emitted by the spacecraft and reflected by the ice sheet or land surface. This laser altimeter measurement provides height of the GLAS instrument above the ice sheet. The geocentric height of the ice surface is computed by differencing the altimeter measurement from the satellite height, which is computed from Precision Orbit Determination (POD) using satellite tracking data.

To achieve the science objectives, especially for measuring the ice-sheet topography, the position of the GLAS instrument should be known with an accuracy of 5 and 20 cm in radial and horizontal components, respectively. This knowledge will be acquired from data collected by the on-board GPS receiver and ground GPS receivers and from the ground-based satellite laser ranging (SLR) data. GPS data will

be the primary tracking data for the ICESat/GLAS POD, and SLR data will be used for POD validation.

1.2   The POD Problem

The problem of determining an accurate ephemeris for an orbiting satellite involves estimating the position and velocity of the satellite from a sequence of observations, which are a function of the satellite position, and velocity. This is accomplished by integrating the equations of motion for the satellite from a reference epoch to each observation time to produce predicted observations. The predicted observations are differenced from the true observations to produce observation residuals. The components of the satellite state (satellite position and velocity and the estimated force and measurement model parameters) at the reference epoch are then adjusted to minimize the observation residuals in a least square sense. Thus, to solve the orbit determination problem, one needs the equations of motion describing the forces acting on the satellite, the observation-state relationship describing the relation of the observed parameters to the satellite state, and the least squares estimation algorithm used to obtain the estimate.

1.3   GPS-based POD

Since the earliest concepts, which led to the development of the Global Positioning System (GPS), it has been recognized that this system could be used for tracking low Earth orbiting satellites. Compared to the conventional ground-based tracking systems, such as the satellite laser ranging or Doppler systems, the GPS

tracking system has the advantage of providing continuous tracking of a low satellite with high precision observations of the satellite motion with a minimal number of ground stations. The GPS tracking system for POD consists of a GPS flight receiver, a global GPS tracking network, and a ground data processing and control system.

1.3.1   Historical Perspective

The GPS tracking system has demonstrated its capability of providing high precision POD products through the GPS flight experiment on TOPEX/Poseidon (T/P) [*Melbourne et al.*, 1994]. Precise orbits computed from the GPS tracking data [*Yunck et al.*, 1994; *Christensen et al.*, 1994; *Schutz et al.*, 1994] are estimated to have a radial orbit accuracy comparable to or better than the precise orbit ephemerides (POE) computed from the combined SLR and DORIS tracking data [*Tapley et al*., 1994] on T/P. When the reduced-dynamic orbit determination technique was employed with the GPS data, which includes process noise accelerations that absorb dynamic model errors after fixing all dynamic model parameters from the fully dynamic approach, there is evidence to suggest that the radial orbit accuracy is better than 3 cm [*Bertiger et al*., 1994].

While GPS receivers have flown on missions prior to T/P, such as Landsat-4 and -5, and Extreme Ultraviolet Explorer, the receivers were single frequency and had high level of ionospheric effects relative to the dual frequency T/P receiver. In addition, the satellite altitudes were 700 km and 500 km, respectively, and the geopotential models available for POD, as they are today, had large errors for

such altitudes. As a result, sub-decimeter radial orbit accuracy could not be achieved for these satellites.

Through the GPS flight experiment on T/P several important lessons on GPS-based POD have been learned. Those include: 1) GPS Demonstration Receiver (GPS/DR) on T/P provides continuous, global, and high precision GPS observable. 2) GPS-based POD produces T/P radial orbit accuracy similar or better than SLR/DORIS. 3) Gravity tuning using GPS measurement was effective [*Tapley et al.*, 1996]. 4) Both reduced-dynamic technique and dynamic approach with extensive parameterization have been shown to reduce orbit errors caused by mismodeling of satellite forces.

1.3.2 *GPS-based POD Strategies*

Several different POD approaches are available using GPS measurements. Those include the kinematic or geometric approach, dynamic approach, and the reduced-dynamic approach.

The kinematic or geometric approach does not require the description of the dynamics except for possible interpolation between solution points for the user satellite, and the orbit solution is referenced to the phase center of the on-board GPS antenna instead of the satellite's center of mass. *Yunck and Wu* [1986] proposed a geometric method that uses the continuous record of satellite position changes obtained from the GPS carrier phase to smooth the position measurements made with pseudorange. This approach assumes the accessibility of P-codes at both the L1 and L2 frequencies. *Byun* [1998] developed a kinematic orbit determination algorithm

using double- and triple-differenced GPS carrier phase measurements. Kinematic solutions are more sensitive to geometrical factors, such as the direction of the GPS satellites and the GPS orbit accuracy, and they require the resolution of phase ambiguities.

The dynamic orbit determination approach [*Tapley*, 1973] requires precise models of the forces acting on user satellite. This technique has been applied to many successful satellite missions and has become the mainstream POD approach. Dynamic model errors are the limiting factor for this technique, such as the geopotential model errors and atmospheric drag model errors, depending on the dynamic environment of the user satellite. With the continuous, global, and high precision GPS tracking data, dynamic model parameters, such as geopotential parameters, can be tuned effectively to reduce the effects of dynamic model error in the context of dynamic approach. The dense tracking data also allows for the frequent estimation of empirical parameters to absorb the effects of unmodeled or mismodeled dynamic error.

The reduced-dynamic approach [*Wu et al*., 1987] uses both geometric and dynamic information and weighs their relative strength by solving for local geometric position corrections using a process noise model to absorb dynamic model errors.

Note that the adopted approach for ICESat/GLAS POD is the dynamic approach with gravity tuning and the reduced-dynamic solutions will be used for validation of the dynamic solutions.

1.4   Outline

This document describes the algorithms for the precise orbit determination (POD) of ICESat/GLAS. Chapter 2 describes the objective for ICESat/GLAS POD algorithm. Chapter 3 summarizes the dynamic models, and Chapter 4 describes the measurement models for ICESat/GLAS. Chapter 5 describes the least squares estimation algorithm and the problem formulation for multi-satellite orbit determination problem. Chapter 6 summarizes the implementation considerations for ICESat/GLAS POD algorithms.

2.0   OBJECTIVE

The objective of the POD algorithm is to determine an accurate position of the center of mass of the spacecraft carrying the GLAS instrument. This position must be expressed in an appropriate Earth-fixed reference frame, such as the International Earth Rotation Service (IERS) Terrestrial Reference Frame (ITRF), but for some applications the position vector must be given in a non-rotating frame, the IERS Celestial Reference Frame (ICRF). Thus, the POD algorithm will provide a data product that consists of time and the (x, y, z) position (ephemeris) of the spacecraft/GLAS center of mass in both the ITRF and the ICRF. The ephemeris will be provided at an appropriate time interval, e.g., 30 sec and interpolation algorithms will enable determination of the position at any time to an accuracy comparable to the numerical integration accuracy. Furthermore, the transformation matrix between ICRF and ITRF will be provided from the POD, along with interpolation algorithm.

3.0   ALGORITHM DESCRIPTION: Orbit

3.1   ICESat/GLAS Orbit Dynamics Overview

Mathematical models employed in the equations of motion to describe the motion of ICESat/GLAS can be divided into three categories: 1) the gravitational forces acting on ICESat/GLAS consist of Earth's geopotential, solid earth tides, ocean tides, planetary third-body perturbations, and relativistic accelerations; 2) the non-gravitational forces consist of drag, solar radiation pressure, earth radiation pressure, and thermal radiation acceleration; and 3) empirical force models that are employed to accommodate unmodeled or mismodeled forces. In this chapter, the dynamic models are described along with the time and reference coordinate systems.

3.2   Equations of Motion, Time and Coordinate Systems

The equations of motion of a near-Earth satellite can be described in an inertial reference frame as follows:

$$\ddot{\overline{r}} = \overline{a}_g + \overline{a}_{ng} + \overline{a}_{emp} \tag{3.2.1}$$

where $\overline{r}$ is the position vector of the center of mass of the satellite, $\overline{a}_g$ is the sum of the gravitational forces acting on the satellite, $\overline{a}_{ng}$ is the sum of the non-gravitational forces acting on the surfaces of the satellite, and $\overline{a}_{emp}$ is the unmodeled forces which act on the satellite due to either a functionally incorrect or incomplete description of the various forces acting on the spacecraft or inaccurate values for the constant parameters which appear in the force model.

3.2.1 Time System

Several time systems are required for the orbit determination problem. From the measurement systems, satellite laser ranging measurements are usually time-tagged in UTC (Coordinated Universal Time) and GPS measurements are time-tagged in GPS System Time (referred to here as GPS-ST). Although both UTC and GPS-ST are based on atomic time standards, UTC is loosely tied to the rotation of the Earth through the application of "leap seconds" to keep UT1 and UTC within a second. GPS-ST is continuous to avoid complications associated with a discontinuous time scale [*Milliken and Zoller*, 1978]. Leap seconds are introduced on January 1 or July 1, as required. The relation between GPS-ST and UTC is

$$GPS\text{-}ST = UTC + n \tag{3.2.2}$$

where n is the number of leap seconds since January 6, 1980. For example, the relation between UTC and GPS-ST in mid-July, 1999, was GPS-ST = UTC + 13 sec. The independent variable of the near-Earth satellite equations of motion (Eq. 3.2.1) is typically TDT (Terrestrial Dynamical Time), which is an abstract, uniform time scale implicitly defined by equations of motion. This time scale is related to the TAI (International Atomic Time) by the relation

$$TDT = TAI + 32.184^s. \tag{3.2.3}$$

The planetary ephemerides are usually given in TDB (Barycentric Dynamical Time) scale, which is also an abstract, uniform time scale used as the independent variable for the ephemerides of the Moon, Sun, and planets. The transformation from the TDB time to the TDT time with sufficient accuracy for most application has been

given by *Moyer* [1981]. For a near-Earth application like ICESat/GLAS, it is unnecessary to distinguish between TDT and TDB. New time systems are under discussion by the International Astronomical Union. This document will be updated with these time systems, as appropriate.

3.2.2   Coordinate System

The inertial reference system adopted for Eq. 3.2.1 for the dynamic model is the ICRF geocentric inertial coordinate system, which is defined by the mean equator and vernal equinox at Julian epoch 2000.0. The Jet Propulsion Laboratory (JPL) DE-405 planetary ephemeris [*Standish*, 1998], which is based on the ICRF inertial coordinate system, has been adopted for the positions and velocities of the planets with the coordinate transformation from barycentric inertial to geocentric inertial.

Tracking station coordinates, atmospheric drag perturbations, and gravitational perturbations are usually expressed in the Earth fixed, geocentric, rotating system, which can be transformed into the ICRF reference frame by considering the precession and nutation of the Earth, its polar motion, and UT1 transformation. The 1976 International Astronomical Union (IAU) precession [*Lieske et al.*, 1977; *Lieske*, 1979] and the 1980 IAU nutation formula [*Wahr*, 1981b; *Seidelmann*, 1982] with the correction derived from VLBI analysis [*Herring et al.*, 1991] will be used as the model of precession and nutation of the Earth. Polar motion and UT1-TAI variations were derived from Lageos (Laser Geodynamics Satellite) laser ranging analysis [*Tapley et al.*, 1985; *Schutz et al.*, 1988]. Tectonic plate motion

for the continental mass on which tracking stations are affixed has been modeled based on the AM0-2 model [*Minster and Jordan*, 1978; *DeMets et al.*, 1990; *Watkins*, 1990]. *Yuan* [1991] provides additional detailed discussion of time and coordinate systems in the satellite orbit determination problem.

3.3 Gravitational Forces

The gravitational forces can be expressed as:

$$\bar{a}_g = \bar{P}_{geo} + \bar{P}_{st} + \bar{P}_{ot} + \bar{P}_{rd} + \bar{P}_n + \bar{P}_{rel} \tag{3.3.1}$$

where

$\bar{P}_{geo}$ = perturbations due to the geopotential of the Earth

$\bar{P}_{st}$ = perturbations due to the solid Earth tides

$\bar{P}_{ot}$ = perturbations due to the ocean tides

$\bar{P}_{rd}$ = perturbations due to the rotational deformation

$\bar{P}_n$ = perturbations due to the Sun, Moon and planets

$\bar{P}_{rel}$ = perturbations due to the general relativity

3.3.1 Geopotential

The perturbing forces of the satellite due to the gravitational attraction of the Earth can be expressed as the gradient of the potential, U, which satisfies the Laplace equation, $\nabla^2 U = 0$:

$$\nabla U = \nabla(U_s + \Delta U_{st} + \Delta U_{ot} + \Delta U_{rd}) = \overline{P}_{geo} + \overline{P}_{st} + \overline{P}_{ot} + \overline{P}_{rd} \qquad (3.3.2)$$

where U_s is the potential due to the solid-body mass distribution, ΔU_{st} is the potential change due to solid-body tides, ΔU_{ot} is the potential change due to the ocean tides, and ΔU_{rd} is the potential change due to the rotational deformations.

The perturbing potential function for the solid-body mass distribution of the Earth, U_s, is generally expressed in terms of a spherical harmonic expansion, referred to as the geopotential, in a body-fixed reference frame as [*Kaula*, 1966; *Heiskanen and Moritz,* 1967]:

$$U_s(r,\phi,\lambda) = \frac{GM_e}{r} + \frac{GM_e}{r}\sum_{l=1}^{\infty}\sum_{m=0}^{l}\left(\frac{a_e}{r}\right)^l \overline{P}_{lm}(\sin\phi)\left[\overline{C}_{lm}\cos m\lambda + \overline{S}_{lm}\sin m\lambda\right]$$

$$(3.3.3)$$

where

GM_e	=	the gravitational constant of the Earth
a_e	=	the mean equatorial radius of the Earth
$\overline{C}_{lm}, \overline{S}_{lm}$	=	normalized spherical harmonic coefficients of degree l and order m
$\overline{P}_{lm}(\sin\varphi)$	=	the normalized associated Legendre function of degree l and order m
r, ϕ, λ	=	radial distance from the center of mass of the Earth, the geocentric latitude, and the longitude of the satellite

To ensure that the origin of spherical coordinates coincides with the center of mass of the Earth, we define $\overline{C}_{10} = \overline{C}_{11} = \overline{S}_{11} = 0$.

3.3.2   Solid Earth Tides

Since the Earth is a non-rigid elastic body, its mass distribution and the shape will be changed under the gravitational attraction of the perturbing bodies, especially the Sun and the Moon. The temporal variation of the free space geopotential induced from solid Earth tides can be expressed as a change in the external geopotential by the following expression [*Wahr*, 1981a; *Dow,* 1988; *Casotto,* 1989].

$$\Delta U_{st} = \frac{GM_e}{a_e^2} \sum_{l=2}^{(3)} \sum_{m=0}^{l} \sum_{k(l,m)} H_k e^{i(\Theta_k + \chi_k)} k_k^0 \left[\left(\frac{a_e}{r} \right)^{l+1} Y_m^l(\phi,\lambda) + k_k^+ \left(\frac{a_e}{r} \right)^{l+3} Y_m^{l+2}(\phi,\lambda) \right]$$

(3.3.4)

where

$$Y_l^m(\phi,\lambda) = (-1)^m \sqrt{\frac{(2l+1)}{4\pi} \frac{(l-m)!}{(l+m)!}} P_{lm}(\sin\phi) e^{im\lambda}$$

$P_{lm}(\sin\phi)$ = the unnormalized associated Legendre function of degree l and order m

H_k = the frequency dependent tidal amplitude in meters (provided in *Cartwright and Tayler* [1971] and *Cartwright and Edden* [1973])

Θ_k, χ_k = Doodson argument and phase correction for constituent k
($\chi_k = 0$, if *l-m* is even; $\chi_k = -\frac{\pi}{2}$, if *l-m* is odd)

k_k^0, k_k^+ = Love numbers for tidal constituent k

r, ϕ, λ = geocentric body-fixed coordinates of the satellite

The summation over *k(l,m)* means that each different *l, m* combination has a unique list of tidal frequencies, *k*, to sum over.

The tidally induced variations in the Earth's external potential can be expressed as variations in the spherical harmonic geopotential coefficients [*Eanes et al*. 1983].

$$\Delta\bar{C}_{lm} = \frac{(-1)^m}{a_e\sqrt{4\pi(2-\delta_{0m})}}\sum_k k_k^0 H_k \begin{cases} \cos\Theta_k, & l-m \quad even \\ \sin\Theta_k, & l-m \quad odd \end{cases}$$

$$\Delta\bar{S}_{lm} = \frac{(-1)^m}{a_e\sqrt{4\pi(2-\delta_{0m})}}\sum_k k_k^0 H_k \begin{cases} -\sin\Theta_k, & l-m \quad even \\ \cos\Theta_k, & l-m \quad odd \end{cases} \qquad (3.3.5)$$

where δ_{0m} is the Kronecker delta; $\Delta\bar{C}_{lm}$ and $\Delta\bar{S}_{lm}$ are the time-varying geopotential coefficients providing the spatial description of the luni-solar tidal effect.

3.3.3   Ocean Tides

The oceanic tidal perturbations due to the attraction of the Sun and the Moon can be expressed as variations in the spherical harmonic geopotential coefficients. The temporal variation of the free space geopotential induced from the ocean tide deformation, ΔU_{ot}, can be expressed as [*Eanes et al.*, 1983]

$$\Delta U_{ot} = 4\pi G\rho_w a_e \sum_k \sum_{l=0}^{\infty}\sum_{m=0}^{l}\sum_{+}^{-} \frac{1+k_l'}{2l+1}\left(\frac{a_e}{r}\right)^{l+1}$$

$$\times\left[C_{klm}^{\pm}\cos(\Theta_k\pm m\lambda) + S_{klm}^{\pm}\sin(\Theta_k\pm m\lambda)\right]P_{lm}(\sin\phi) \qquad (3.3.6)$$

where ρ_w is the mean density of sea water, k is the ocean tide constituent index, k_l' is the load Love number of degree l, $C^{\pm}_{klm}$ and $S^{\pm}_{klm}$ are the unnormalized prograde and retrograde tide coefficients, and Θ_k is the Doodson argument for constituent k.

The above variations in the Earth's external potential due to the ocean tide can be expressed as variations in the spherical harmonic geopotential coefficients as follows [*Eanes et al.* 1983].

$$\Delta \bar{C}_{lm} = F_{lm} \sum_k A_{klm}$$

$$\Delta \bar{S}_{lm} = F_{lm} \sum_k B_{klm} \tag{3.3.7}$$

where F_{lm}, A_{klm}, and B_{klm} are defined as

$$F_{lm} = \frac{4\pi a_e^2 \rho_w}{M_e} \sqrt{\frac{(l+m)!}{(l-m)!(2l+1)(2-\delta_{0m})}} \left(\frac{1+k_l'}{2l+1}\right) \tag{3.3.8}$$

and

$$\begin{bmatrix} A_{klm} \\ B_{klm} \end{bmatrix} = \begin{bmatrix} (C^+_{klm} + C^-_{klm}) \\ (S^+_{klm} - S^-_{klm}) \end{bmatrix} \cos\Theta_k + \begin{bmatrix} (S^+_{klm} + S^-_{klm}) \\ (C^-_{klm} - C^+_{klm}) \end{bmatrix} \sin\Theta_k \tag{3.3.9}$$

3.3.4 Rotational Deformation

Since the Earth is elastic and includes a significant fluid component, changes in the angular velocity vector will produce a variable centrifugal force, which consequently deforms the Earth. This deformation, which is called "rotational deformation", can be expressed as the change of the centrifugal potential, U_c [*Lambeck*, 1980] given by

$$U_c = \frac{1}{3}\omega^2 r^2 + \Delta U_c \tag{3.3.10}$$

where

$$\Delta U_c = \frac{r^2}{6}(\omega_1^2 + \omega_2^2 - 2\omega_3^2)\, P_{20}(\sin\phi)$$

$$-\frac{r^2}{3}(\omega_1\omega_3\cos\lambda + \omega_2\omega_3\sin\lambda)\, P_{21}(\sin\phi)$$

$$+\frac{r^2}{12}\left[(\omega_2^2-\omega_1^2)\cos2\lambda - 2\omega_1\omega_2\sin2\lambda\right] P_{22}(\sin\phi) \tag{3.3.11}$$

and $\omega_1 = \Omega m_1$, $\omega_2 = \Omega m_2$, $\omega_3 = \Omega(1+m_3)$, and $\omega^2 = (\omega_1^2+\omega_2^2+\omega_3^2)$. Ω is the mean angular velocity of the Earth, m_i are small dimensionless quantities which are related to the polar motion and the Earth rotation parameters by the following expressions:

$$m_1 = x_p$$

$$m_2 = -y_p \tag{3.3.12}$$

$$m_3 = \frac{d\,(UT1\text{-}TAI)}{d\,(TAI)}$$

The first term of Eq. (3.3.10) is negligible in the variation of the geopotential, thereby the variation of the free space geopotential outside of the Earth due to the rotational deformation can be written as

$$\Delta U_{rd} = \left(\frac{a_e}{r}\right)^3 k_2\, \Delta U_c(a_e) \tag{3.3.13}$$

The above variations in the Earth's external potential due to the rotational deformation can be expressed as variations in the spherical harmonic geopotential coefficients as follows.

$$\Delta C_{20} = \frac{a_e^3}{6GM_e}\left[m_1{}^2+m_2{}^2-2(1+m_3)^2\right]\Omega^2 k_2 \approx \frac{-a_e^3}{3GM_e}(1+2m_3)\Omega^2 k_2$$

$$\Delta C_{21} = \frac{-a_e^3}{3GM_e} \, m_1(1+m_3)\Omega^2 k_2 \approx \frac{-a_e^3}{3GM_e} \, m_1\Omega^2 k_2$$

$$\Delta S_{21} = \frac{-a_e^3}{3GM_e} \, m_2(1+m_3)\Omega^2 k_2 \approx \frac{-a_e^3}{3GM_e} \, m_2\Omega^2 k_2 \qquad (3.3.14)$$

$$\Delta C_{22} = \frac{a_e^3}{12GM_e} \, (m_2{}^2-m_1{}^2)\Omega^2 k_2 \approx 0$$

$$\Delta S_{22} = \frac{-a_e^3}{6GM_e} \, (m_2 m_1)\Omega^2 k_2 \approx 0$$

As a consequence of Eqs. (3.3.2), (3.3.3), (3.3.4), (3.3.6), and (3.3.13), the resultant gravitational potential for the Earth can be expressed as

$$U(r,\phi,\lambda) = \frac{GM_e}{r} + \frac{GM_e}{r} \sum_{l=1}^{\infty} \sum_{m=0}^{l} \left(\frac{a_e}{r}\right)^l \overline{P}_{lm}\left(\sin\phi\right)$$

$$\times \left[\left(\overline{C}_{lm}+\Delta\overline{C}_{lm}\right)\cos m\lambda + \left(\overline{S}_{lm}+\Delta\overline{S}_{lm}\right)\sin m\lambda\right] \qquad (3.3.15)$$

where both the solid Earth and oceans contribute to the periodic variations $\Delta\overline{C}_{lm}$ and $\Delta\overline{S}_{lm}$.

3.3.5 N-Body Perturbation

The gravitational perturbations of the Sun, Moon and other planets can be modeled with sufficient accuracy using point mass approximations. In the geocentric inertial coordinate system, the N-body accelerations can be expressed as:

$$\overline{P}_n = \sum_i GM_i \left[\frac{\overline{r}_i}{r_i^3} - \frac{\overline{\Delta}_i}{\Delta_i^3}\right] \qquad (3.3.16)$$

where

G	=	the universal gravitational constant
M_i	=	mass of the i-th perturbing body
$\bar{r}_i$	=	position vector of the i-th perturbing body in geocentric inertial coordinates
$\bar{\Delta}_i$	=	position vector of the i-th perturbing body with respect to the satellite

The values of $\bar{r}_i$ can be obtained from the Jet Propulsion Laboratory Development Ephemeris-405 (JPL DE-405) [*Standish*, 1998].

3.3.6 *General Relativity*

The general relativistic perturbations on the near-Earth satellite can be modeled as [*Huang et al.*, 1990; *Ries et al.*, 1988],

$$\bar{P}_{rel} = \frac{GM_e}{c^2 r^3} \left\{ \left[(2\beta + 2\gamma) \frac{GM_e}{r} - \gamma (\vec{r} \cdot \dot{\vec{r}}) \right] \bar{r} + (2 + 2\gamma)(\vec{r} \cdot \dot{\vec{r}}) \dot{\vec{r}} \right\}$$

$$+ 2 (\bar{\Omega} \times \dot{\vec{r}}) \tag{3.3.17}$$

$$+ L (1 + \gamma) \frac{GM_e}{c^2 r^3} \left[\frac{3}{r^2} (\vec{r} \times \dot{\vec{r}})(\vec{r} \cdot \bar{J}) + (\vec{r} \times \bar{J}) \right]$$

where

$$\bar{\Omega} \approx \left(\frac{1+\gamma}{2} \right) (\dot{\bar{R}}_{ES}) \times \left[\frac{-GM_s \bar{R}_{ES}}{c^2 R_{ES}^3} \right]$$

c	=	the speed of light in the geocentric frame
$\bar{r}, \dot{\vec{r}}$	=	the geocentric satellite position and velocity vectors
$\bar{R}_{ES}$	=	the position of the Earth with respect to the Sun

GM_e, GM_s = the gravitational constants for the Earth and the Sun, respectively

$\bar{J}$　　　　= the Earth's angular momentum per unit mass

　　　　($|\bar{J}| = 9.8 \times 10^8$ m²/sec)

L　　　　= the Lense-Thirring parameter

β, γ　　　　= the parameterized post-Newtonian (PPN) parameters

The first term of Eq. (3.3.17) is the Schwarzschild motion [*Huang et al.*, 1990] and describes the main effect on the satellite orbit with the precession of perigee. The second term of Eq. (3.3.17) is the effect of geodesic (or de Sitter) precession, which results in a precession of the orbit plane [*Huang and Ries*, 1987]. The last term of Eq. (3.3.17) is the Lense-Thirring precession, which is due to the angular momentum of the rotating Earth and results in, for example, a 31 mas/yr precession in the node of the Lageos orbit [*Ciufolini*, 1986].

3.4　Nongravitational Forces

The non-gravitational forces acting on the satellite can be expressed as:

$$\bar{a}_{ng} = \bar{P}_{drag} + \bar{P}_{solar} + \bar{P}_{earth} + \bar{P}_{thermal} \tag{3.4.1}$$

where

$\bar{P}_{drag}$　　　　= perturbations due to the atmospheric drag

$\bar{P}_{solar}$　　　　= perturbations due to the solar radiation pressure

$\bar{P}_{earth}$　　　　= perturbations due to the Earth radiation pressure

$\bar{P}_{thermal}$　　　　= perturbations due to the thermal radiation

Since the surface forces depend on the shape and orientation of the satellite, the models are satellite dependent. In this section, however, general models are described.

3.4.1 Atmospheric Drag

A near-Earth satellite of arbitrary shape moving with some velocity $\overline{v}$ in an atmosphere of density ρ will experience both lift and drag forces. The lift forces are small compared to the drag forces, which can be modeled as [*Schutz and Tapley*, 1980b]

$$\overline{P}_{drag} = -\frac{1}{2} \rho \left(\frac{C_d A}{m} \right) v_r \overline{v}_r \tag{3.4.2}$$

where

ρ = the atmospheric density

$\overline{v}_r$ = the satellite velocity relative to the atmosphere

v_r = the magnitude of $\overline{v}_r$

m = mass of the satellite

C_d = the drag coefficient for the satellite

A = the cross-sectional area of the main body perpendicular to $\overline{v}_r$

The parameter $\dfrac{C_d A}{m}$ is sometimes referred to as the ballistic coefficient. When more detailed modeling is needed, the drag force on any specific spacecraft surface, for example, the solar panel, can be modeled as

$$\overline{P}_{paneld} = -\frac{1}{2} \rho \left(\frac{C_{dp} |A_p \cos\gamma|}{m} \right) v_r \overline{v}_r \tag{3.4.3}$$

where

C_{dp} = the drag coefficient for the solar panel

A_p = the solar panel's area

γ = the angle between the solar panel surface normal unit vector, $\hat{n}$, and satellite velocity vector, $\overline{v}_r$ (i.e. $\cos\gamma = \hat{n} \cdot \left(\dfrac{\overline{v}_r}{v_r}\right)$)

$|A_p\cos\gamma|$ = the effective solar panel cross sectional area perpendicular to $\overline{v}_r$

There are a number of empirical atmospheric density models used for computing the atmospheric density. These include the Jacchia 71 [*Jacchia*, 1971], Jacchia 77 [*Jacchia*, 1977], the Drag Temperature Model (DTM) [*Barlier et al.*, 1977], and MSIS-90 [*Hedin*, 1991]. The density computed by using any of these models could be in error anywhere from 10% to over 200% depending on solar activity [*Shum et al.*, 1986]. To account for the deviations in the computed values of density from the true density, the computed values of density, ρ_c, can be modified by using empirical parameters which are adjusted in the orbit solution. Once-per-revolution density correction parameters [*Elyasberg et al.*, 1972; *Shum et al.*, 1986] have been shown to be especially effective for these purposes such that

$$\rho = \rho_c\left[1 + C_1 \cos(M+\omega) + C_2 \sin(M+\omega)\right] \tag{3.4.4}$$

where

C_1, C_2 = the once-per-revolution density correction coefficients

M = mean anomaly of the satellite

ω = argument of perigee of the satellite

3.4.2   Solar Radiation Pressure

The Sun emits a nearly constant amount of photons per unit of time. At a mean distance of 1 A.U. from the Sun, this radiation pressure is characterized as a momentum flux having an average value of 4.56×10^{-6} N/m^2. The direct solar radiation pressure from the Sun on a satellite is modeled as [*Tapley and Ries*, 1987]

$$\overline{P}_{solar} = -P (1 + \eta) \frac{A}{m} v \, \hat{u} \qquad (3.4.5)$$

where

P	=	the momentum flux due to the Sun
η	=	reflectivity coefficient of the satellite
A	=	the cross-sectional area of the satellite normal to the Sun
m	=	mass of the satellite
v	=	the eclipse factor ($v = 0$ if the satellite is in full shadow, $v = 1$ if the satellite is in full Sun, and $0 < v < 1$ if the satellite is in partial shadow)
$\hat{u}$	=	the unit vector pointing from the satellite to the Sun

Similarly, the solar radiation pressure perturbation on an individual satellite surface, like the satellite's solar panel, can be modeled as

$$\overline{P}_{panels} = -P \, v \frac{|A_p \cos\gamma|}{m} \left(\hat{u} + \eta_p \, \hat{n}\right) \qquad (3.4.6)$$

where

A_p	=	the solar panel area
$\hat{n}$	=	the surface normal unit vector of the solar panel
γ	=	the angle between the solar panel surface normal unit vector, $\hat{n}$, and satellite-Sun unit vector, $\hat{u}$ (i.e. $\cos \gamma = \hat{u} \cdot \hat{n}$)

$|A_p \cos\gamma|$ = the effective solar panel cross sectional area perpendicular to $\hat{u}$

The reflectivity coefficient, η, represents the averaged effect over the whole satellite rather than the actual surface reflectivity. Conical or cylindrical shadow models for the Earth and the lunar shadow are used to determine the eclipse factor, ν. Since there are discontinuities in the solar radiation perturbation across the shadow boundary, numerical integration errors occur for satellites, which are in the shadowing region. The modified back differences (MBD) method [*Anderle*, 1973] can be implemented to account for these errors [*Lundberg*, 1985; *Feulner*, 1990].

3.4.3   Earth Radiation Pressure

Not only the direct solar radiation pressure, but also the radiation pressure imparted by the energy flux of the Earth should be modeled for the precise orbit determination of any near-Earth satellite. The Earth radiation pressure model can be summarized as follows [*Knocke and Ries*, 1987; *Knocke*, 1989].

$$\overline{P}_{earth} = (1+\eta_e)A'\frac{A_c}{mc}\sum_{j=1}^{N}\left[(\tau a E_s \cos\theta_s + eM_B)\hat{r}\right]_j \qquad (3.4.7)$$

where

η_e = satellite reflectivity for the Earth radiation pressure

A' = the projected, attenuated area of a surface element of the Earth

A_c = the cross sectional area of the satellite

m = the mass of the satellite

c = the speed of light

τ = 0 if the center of the element j is in darkness

1 if the center of the element *j* is in daylight

a, e = albedo and emissivity of the element *j*

E_s = the solar momentum flux density at 1 A.U.

θ_s = the solar zenith angle

M_B = the exitance of the Earth

$\hat{r}$ = the unit vector from the center of the element *j* to the satellite

N = the total number of segments

This model is based on *McCarthy and Martin* [1977].

The nominal albedo and emissivity models can be represented as

$$a = a_0 + a_1 P_{10}(\sin\phi) + a_2 P_{20}(\sin\phi) \tag{3.4.8}$$

$$e = e_0 + e_1 P_{10}(\sin\phi) + e_2 P_{20}(\sin\phi) \tag{3.4.9}$$

where

$$a_1 = c_0 + c_1 \cos\omega(t\text{-}t_0) + c_2 \sin\omega(t\text{-}t_0) \tag{3.4.10}$$

$$e_1 = k_0 + k_1 \cos\omega(t\text{-}t_0) + k_2 \sin\omega(t\text{-}t_0) \tag{3.4.11}$$

and

P_{10}, P_{20} = the first and second degree Legendre polynomial

ϕ = the latitude of the center of the element on the Earth's surface

ω = frequency of the periodic terms (period = 365.25 days)

$t\text{-}t_0$ = time from the epoch of the periodic term

This model, based on analyses of Earth radiation budgets by *Stephens et al.* [1981], characterizes both the latitudinal variation in Earth radiation and the seasonally dependent latitudinal asymmetry.

3.4.4   Thermal Radiation Perturbation

Since the temperatures of the satellite's surface are not uniform due to the internal and external heat fluxes, there exists a force due to a net thermal radiation imbalance. This perturbation depends on the shape, the thermal property, the pattern of thermal dumping, the orbit characteristics, and the thermal environment of the satellite as a whole. This modeling can be quite complex. For example, if a satellite has active louvers for heat dissipation, the thermal force can have specular characteristics whereas the heat loss to space from a flat plat is normally diffusive. Even a clean, perfect spherical satellite like Lageos [*Ries*, 1989] has been found to have a range of detectable thermally induced forces. It is observed for GPS satellites that there are unexplained forces in the body-fixed +*Y* or -*Y* direction, that is along solar panel rotation axis, which causes unmodeled accelerations [*Fliegel et al.,* 1992] believed to be of thermal origin. This acceleration is referred to as the "Y-bias". Possible causes of the Y-bias are solar panel axis misalignment, solar sensor misalignment, and the heat generated in the GPS satellite body, which is radiated preferentially from louvers on the +*Y* side. Since this Y-bias perturbation is not predictable, it can be modeled as

$$\overline{P}_{ybias} \; = \; \alpha \cdot \; \widehat{u}_Y \qquad\qquad\qquad (3.4.12)$$

where $\widehat{u}_Y$ is a unit vector in the *Y*-direction, and the scale factor, α, is estimated for each GPS satellite.   Models, which are satellite-specific, are required to properly

account for these effects depending on the orbit accuracy needed within a given application.

3.4.5   *GPS Solar Radiation Pressure Models*

At the 20,000-km altitude of GPS satellite, solar radiation is the dominant non-gravitational force acting on the spacecraft. Several GPS solar radiation pressure models are currently available, and two of those models are summarized in this section.

Rockwell International Corporation, which was the spacecraft contractor for the Block I and II GPS satellites, developed GPS satellite solar radiation pressure models, known as ROCK4 for Block I, and ROCK42 for Block II [*Fliegel et al.*, 1992]. These models treat a spacecraft as a set of flat or cylindrical surfaces. Diffusive and specular forces acting on each surface are computed and summed in the spacecraft body-fixed coordinate system. The +*Z* direction is toward the satellite-Earth vector. The +*Y* direction is along one of the solar panel center beams. The satellite is maneuvered so that the *X*-axis will be kept in the plane defined by the Earth, the Sun and the satellite. As a result, the solar radiation pressure forces are confined in the *X-Z* plane, since the *Y*-axis is perpendicular to the Earth, Sun and the satellite plane. The ROCK4 model also provides solar radiation formulas for the *X*- and *Z*- acceleration components as a function of the angle between the Sun and the +*Z*-axis, e.g. T10 for Block I, and T20 for Block II GPS satellites [*Fliegel et al.*, 1992].

Recently the Center of Orbit Determination in Europe (CODE) developed a solar radiation pressure (RPR) model by analyzing 5.5 years of GPS orbit solutions

[*Springer et al.*, 1998]. The RPR model is represented by eighteen orbit parameters in two different coordinate systems. Those are satellite body-fixed coordinate system described above, and the Sun-oriented reference system, which consists of the *D*-, *Y*-, and *B*-axis [*Beutler et al.*, 1994]. The *D*-axis is the satellite-Sun direction positive towards the Sun, *Y*-axis is identical to the ROCK4 *Y*-axis, and *B*-axis completes a right-handed system. The orbit parameters include three constant terms in the *D*-, *Y*-, and *B*-direction, a once-per-revolution term in the *Z*-direction, and once- and three times-per-revolution terms in the *X*-direction. The solar radiation acceleration is expressed as

$$a_D = D_0 + D_{C2}\,cos(2\beta) + D_{C4}\,cos(4\beta)$$

$$a_Y = Y_0 + Y_C\,cos(2\beta)$$

$$a_B = B_0 + B_C\,cos(2\beta) \tag{3.4.13}$$

$$a_Z = \{Z_0 + Z_{C2}\,cos(2\beta) + Z_{S2}\,sin(2\beta)$$

$$+Z_{C4}\,cos(4\beta) + Z_{S4}\,sin(4\beta)\}sin(u - u_0)$$

$$a_X = \{X_{10} + X_{1C}\,cos(2\beta) + X_{1S}\,sin(2\beta)\}sin(u - u_0)$$

$$+\{X_{30} + X_{3C}\,cos(2\beta) + X_{3S}\,sin(2\beta)\}\,sin(3u - u_0)$$

where *u* is the argument of latitude of satellite in the orbit plane, *u₀* is the latitude of the Sun in the orbit plane, and *β* is the angular distance between the orbit plane and the Sun.

3.4.6 ICESat/GLAS "Box-Wing" Model

For modeling of non-gravitational perturbations on T/P, the "box-wing" model or the so-called macro-model [*Marshall et al.*, 1992] was developed based on a thermal analysis of the spacecraft [*Antreasian and Rosborough*, 1992]. In the macro-model, the spacecraft main body and the solar panel are represented by a simple geometric model, a box and a wing, and the solar radiation and the thermal forces are computed for each surface and summed over the surfaces. For example, the solar radiation acceleration for the macro-model is computed using the following equation [*Milani et al.*, 1987].

$$\overline{P}_{solar} = -P \frac{\alpha \cdot v}{m} \sum_{i=1}^{nface} A_i \cos\theta_i \left[2(\frac{\delta_i}{3} + \rho_i \cos\theta_i)\hat{n}_i + (1-\rho_i)\hat{s} \right] \qquad (3.4.14)$$

where

$\overline{P}_{solar}$	= the solar radiation pressure acceleration
P	= the momentum flux due to the Sun
α	= the scale factor of the acceleration
v	= the eclipse factor (0 for full shadow, 1 for full Sun)
m	= mass of the satellite
A_i	= surface area of the i-th plate
θ_i	= angle between surface normal and satellite-Sun vector for i-th plate
$\hat{n}_i$	= surface normal unit vector for i-th plate
$\hat{s}$	= satellite-Sun unit vector
δ_i	= specular reflectivity for i-th plate

ρ_i = diffusive reflectivity for i-th plate

nface = total number of plates in the model

A similar model is being developed for the ICESat/GLAS satellite, and the model parameters, including the specular and diffusive reflectivity coefficients, will be tuned using the tracking data.

3.5 Empirical Forces

To account for the unmodeled forces, which act on the satellite or for incorrect force models, some empirical parameters are customarily introduced in the orbit solution. These include the empirical tangential perturbation and the one-cycle-per-orbital-revolution (1cpr) force in the radial, transverse, and normal directions [*Colombo*, 1986; *Colombo*, 1989]. Especially for satellites like ICESat/GLAS which are tracked continuously with high precision data, introduction of these parameters can significantly reduce orbit errors occurring at the 1cpr frequency and in the along track direction [*Rim et al.*, 1996].

3.5.1 Empirical Tangential Perturbation

Unmodeled forces in the tangential direction, either along the inertial velocity or along the body-fixed velocity, may be estimated by using empirical models during the orbit determination process. This tangential perturbation can be modeled empirically as

$$\overline{P}_{tangen} \; = \; C_t \, \widehat{u}_t \tag{3.5.1}$$

where

C_t = empirical tangential parameter

$\widehat{u}_t$ = the unit vector in the tangential direction (along inertial velocity

                    or body-fixed velocity)

Such forces are estimated when it is believed that there are mismodeled or unmodeled non-conservative forces in the tangential direction. A set of piecewise constants, C_t, can be estimated to account for these unmodeled tangential perturbations.

3.5.2   *Once-per Revolution RTN Perturbation*

Unmodeled perturbations in the radial, transverse, and normal directions can be modeled as

$$\overline{P}_{rtn} \; = \; \begin{bmatrix} P_r \\ P_t \\ P_n \end{bmatrix} = \begin{bmatrix} C_r \cos u + S_r \sin u \\ C_t \cos u + S_t \sin u \\ C_n \cos u + S_n \sin u \end{bmatrix} \tag{3.5.2}$$

where

P_r = one-cycle-per-revolution radial perturbation

P_t = one-cycle-per-revolution transverse perturbation

P_n = one-cycle-per-revolution normal perturbation

u = the argument of latitude of the satellite

C_r, S_r = the one-cycle-per-revolution radial parameters

C_t, S_t = the one-cycle-per-revolution transverse parameters

C_n, S_n = the one-cycle-per-revolution normal parameters

These empirical perturbations, which are computed in the radial, transverse, and normal components, are transformed into the geocentric inertial components. These parameters are introduced as needed with complete or subsets of empirical terms being used.

4.0   ALGORITHM DESCRIPTION: Measurements

4.1   ICESat/GLAS Measurements Overview

The GPS measurements will be the primary measurement type for the ICESat/GLAS POD, while the laser range measurement will serve as a secondary source of verification and evaluation of the GPS-based ICESat/GLAS POD product. In this chapter, the mathematical models of the GPS and laser range measurements are discussed.

4.2   GPS Measurement Model

The GPS measurements are ranges, which are computed from measured time or phase differences between received signals and receiver generated signals. Since these ranges are biased by satellite and receiver clock errors, they are called pseudoranges.   In this section, code pseudorange (PR) measurements, phase pseudorange measurements (PPR), double-differenced high-low phase pseudorange measurements (DDHL) which involve one ground station, two GPS satellites, and one low Earth orbiting satellite, are discussed. Consult *Hofmann-Wellenhof et al.* [1992] and *Remondi* [1984] for more discussion of GPS measurement models.

4.2.1   Code Pseudorange Measurement

The PR measurement, $\rho^c{}_{PR}$, can be modeled as follows,

$$\rho^c{}_{PR} = \rho - c \cdot \delta t_t + c \cdot \delta t_r + \delta\rho_{trop} + \delta\rho_{iono} + \delta\rho_{rel} \qquad (4.2.1)$$

where ρ is the slant range between the GPS satellite and the receiver receiving the GPS signal, c is the speed of light, δt_t is the GPS satellite's clock error, δt_r is the receiver's clock error, $\delta\rho_{trop}$ is the tropospheric path delay, $\delta\rho_{iono}$ is the ionospheric path delay, and $\delta\rho_{rel}$ is the correction for relativistic effects.

4.2.2   Phase Pseudorange Measurement

The carrier phase measurement between a GPS satellite and a ground station can be modeled as follows,

$$\phi^{c\,j}_i(t_{R_i}) \;=\; \phi^j(t_{T_i}) - \phi_i(t_{R_i}) + N_i^j(t_{0_i}) \tag{4.2.2a}$$

where t_{R_i} is the receive time at the i-th ground receiver, t_{T_i} is the transmit time of the j-th satellite's phase being received by the i-th receiver at t_{R_i}, $\phi^{c\,j}_i(t_{R_i})$ is the computed phase difference between the j-th GPS satellite and i-th ground receiver at t_{R_i}, $\phi^j(t_{T_i})$ is the phase of j-th GPS satellite signal received by i-th receiver, $\phi_i(t_{R_i})$ is the phase of i-th ground receiver at t_{R_i}, t_{0_i} is the initial epoch of the i-th receiver, and $N_i^j(t_{0_i})$ is the integer bias which is unknown and is often referred to as an "ambiguity bias". Similarly, the carrier phase measurement between a GPS satellite and a low satellite can be modeled as follows,

$$\phi^{c\,j}_u(t_{R_u}) \;=\; \phi^j(t_{T_u}) - \phi_u(t_{R_u}) + N_u^j(t_{0_u}) \tag{4.2.2b}$$

where t_{R_u} is the received time of the on-board receiver of the user satellite, t_{T_u} is the transmit time of the j-th satellite's phase being received by the user satellite at t_{R_u}, $\phi^{c\,j}_u(t_{R_u})$ is the computed phase difference between j-th GPS satellite and the user satellite at t_{R_u}, $\phi^j(t_{T_u})$ is the phase of j-th GPS satellite signal received by the user

satellite, $\phi_u(t_{R_u})$ is the phase of the user satellite at t_{R_u}, t_{0_u} is the initial epoch of the user satellite, and $N_u{}^j(t_{0_u})$ is the unknown integer bias.

The signal transmit time of the j-th GPS satellite can be related to the signal receive time by

$$t_{T_i}{}^j = t_{R_i} - (\rho_i{}^j(t_{R_i})/c) - \delta t_{\phi_i}{}^j \qquad (4.2.3a)$$

$$t_{T_u}{}^j = t_{R_u} - (\rho_u{}^j(t_{R_u})/c) - \delta t_{\phi_u}{}^j \qquad (4.2.3b)$$

where $\rho_i{}^j$ is the geometric line of sight range between j-th GPS satellite and i-th ground receiver, $\rho_u{}^j$ is the slant range between j-th GPS satellite and the on-board receiver of the user satellite, $\delta t_{\phi_i}{}^j$ is the sum of ionospheric delay, tropospheric delay, and relativistic effect on the signal traveling from j-th GPS satellite to i-th ground receiver, $\delta t_{\phi_u}{}^j$ is the sum of ionospheric path delay, tropospheric path delay, and relativistic effect on the signal traveling from j-th satellite to the on-board receiver of the user satellite. Since the time tag, t_i or t_u, of the measurement is in the receiver time scale which has some clock error, the true receive times are

$$t_{R_i} = t_i - \delta t_{c_i} \qquad (4.2.4a)$$

$$t_{R_u} = t_u - \delta t_{C_u} \qquad (4.2.4b)$$

where δt_{c_i} is the clock error of the i-th ground receiver at t_{R_i} and δt_{c_u} is the clock error of the on-board receiver of the user satellite at t_{R_u}. Since the satellite oscillators and the receiver oscillators are highly stable clocks, the (1σ) change of the frequency over the specified period, $\frac{\Delta f}{f}$, is on the order of 10^{-12}. With such high stability, the linear approximation of $\phi(t + \delta t) = \phi(t) + f \cdot \delta t$ can be used for δt which is usually less

than 1 second. By substituting Eqs. (4.2.3a) and (4.2.4a) into Eq. (4.2.2a), and neglecting higher order terms, Eq. (4.2.2a) becomes

$$\phi^{c\,j}_i(t_{R_i}) = \phi^j(t_i) - f^j \cdot [\, \delta t_{c_i} + \rho^j_i(t_{R_i})/c + \delta t^j_{\phi_i} \,]$$

$$- \phi_i(t_i) + f_i\, \delta t_{c_i} + N^j_i(t_{0_i}) \qquad (4.2.5a)$$

Similarly, the phase measurement between the j-th GPS satellite and the user satellite can be modeled as follows,

$$\phi^{c\,j}_u(t_{R_u}) = \phi^j(t_u) - f^j \cdot [\, \delta t_{c_u} + \rho^j_u(t_{R_u})/c + \delta t^j_{\phi_u} \,]$$

$$- \phi_u(t_u) + f_u\, \delta t_{c_u} + N^j_u(t_{0_u}) \qquad (4.2.5b)$$

By multiplying a negative nominal wavelength, $-\lambda = -c / f_0$, where f_0 is the nominal value for both the transmit frequency of the GPS signal and the receiver mixing frequency, Eq. (4.2.5a) becomes the phase pseudorange measurement,

$$PPR^{c\,j}_i = \frac{f^j}{f_0} \rho^j_i(t_{R_i}) + \frac{f^j}{f_0} \delta\rho^j_{\phi_i} + \frac{f^j}{f_0} c\, \delta t_{c_i} - \frac{f_i}{f_0} c\, \delta t_{c_i}$$

$$- \frac{c}{f_0} \cdot \left[\phi^j(t_i) - \phi_i(t_i) \right] + C^j_i \qquad (4.2.6)$$

where $\delta\rho^j_{\phi_i} = c\, \delta t^j_{\phi_i}$ and $C^j_i = -\left(\frac{c}{f_0}\right) \cdot N^j_i$.

The first term of second line of Eq. (4.2.6) can be expanded using the following relations:

$$\phi^j(t_i) - \phi_i(t_i) = \phi^j(t_0) - \phi_i(t_0) + \int_{t_0}^{t_i} \left(f^j - f_i\right) dt \qquad (4.2.7)$$

However, $\phi^j(t_0) - \phi_i(t_0) = f^j \delta t^j_c(t_0) - f_i\, \delta t_{c_i}(t_0)$, which is the time difference between the satellite and the receiver clocks at the first data epoch, t_0. And

$\displaystyle\int_{t_0}^{t_i} \left(f^j - f_i\right) dt$ is the total number of cycles the two oscillators have drifted apart over the interval from t_0 to t_i. According to *Remondi* [1984], this is equivalent to the statement that the two clocks have drifted apart, timewise, by amount $\left[\delta t_c^{\,j}(t_i) - \delta t_{c_i}(t_i)\right] - \left[\delta t_c^{\,j}(t_0) - \delta t_{c_i}(t_0)\right]$. Thus,

$$\phi^j(t_i) - \phi_i(t_i) = f^j \cdot \delta t_c^{\,j} - f_i \cdot \delta t_{c_i} \tag{4.2.8}$$

After substituting Eq. (4.2.8), Eq. (4.2.6) becomes,

$$PPR^{c\,j}_{\,i} = \frac{f^j}{f_0}\rho_i^j(t_{R_i}) + \frac{f^j}{f_0}\delta\rho_{\phi_i}^{\,j} - \frac{f^j}{f_0}c\ \delta t_c^{\,j} + \frac{f^j}{f_0}c\ \delta t_{c_i} + C_i^j \tag{4.2.9a}$$

Similarly, the phase pseudorange between j-th satellite and a user satellite can be written as,

$$PPR^{c\,j}_{\,u} = \frac{f^j}{f_0}\rho_u^j(t_{R_u}) + \frac{f^j}{f_0}\delta\rho_{\phi_u}^{\,j} - \frac{f^j}{f_0}c\ \delta t_c^{\,j} + \frac{f^j}{f_0}c\ \delta t_{c_u} + C_u^j \tag{4.2.9b}$$

Since the GPS satellites have highly stable oscillators, which have 10^{-11} or 10^{-12} clock drift rate, the frequencies of those clocks usually stay close to the nominal frequency, f_0. If the frequencies are expressed as $f^j = f_0 + \Delta f^j$, where Δf is clock frequency offset from the nominal value, Eqs. (4.2.9a) and (4.2.9b) become as follows after ignoring negligible terms:

$$PPR^{c\,j}_{\,i} = \rho_i^j(t_{R_i}) + \delta\rho_{\phi_i}^{\,j} - c\ \delta t_c^{\,j} + c\ \delta t_{c_i} + C_i^j \tag{4.2.10a}$$

$$PPR^{c\,j}_{\,u} = \rho_u^j(t_{R_u}) + \delta\rho_{\phi_u}^{\,j} - c\ \delta t_c^{\,j} + c\ \delta t_{c_u} + C_u^j \tag{4.2.10b}$$

Note that $\rho_i^j(t_{R_i})$ and $\rho_u^j(t_{R_u})$ could be expanded as

$$\rho_i^j(t_{R_i}) = \rho_i^j(t_i) - \dot{\rho}_i^j\ \delta t_{c_i} \tag{4.2.11a}$$

$$\rho_u{}^j(t_{R_u}) \; = \; \rho_u{}^j(t_u) \; - \; \dot{\rho}_u{}^j \; \delta t_{c_u} \tag{4.2.11b}$$

Thus, Eqs. (4.2.10a) and (4.2.10b) become

$$PPR^c{}_i{}^j \; = \; \rho_i{}^j(t_i) \; + \; \delta\rho_{\phi_i}{}^j \; - \; c \; \delta t_c{}^j \; + \; c \; \delta t_{c_i} \; - \; \dot{\rho}_i{}^j \; \delta t_{c_i} \; + \; C_i{}^j \tag{4.2.12a}$$

$$PPR^c{}_u{}^j \; = \; \rho_u{}^j(t_u) \; + \; \delta\rho_{\phi_u}{}^j \; - \; c \; \delta t_c{}^j \; + \; c \; \delta t_{c_u} \; - \; \dot{\rho}_u{}^j \; \delta t_{c_u} \; + \; C_u{}^j \tag{4.2.12b}$$

Eq. (4.2.12a) is the phase pseudorange measurement between a ground receiver and a GPS satellite, and Eq. (4.2.12b) is the phase pseudorange measurement between a GPS satellite and a user satellite. Note that the clock errors would be estimated for each observation epoch.

4.2.3   Double-Differenced High-Low Phase Pseudorange Measurement

By subtracting Eq. (4.2.2b) from Eq. (4.2.2a), a single-differenced high-low phase measurement can be formed as follows,

$$SDHLP^c{}_i{}^j{}_u \; = \; \phi^c{}_i{}^j(t_{R_i}) \; - \; \phi^c{}_u{}^j(t_{R_u}) \tag{4.2.13}$$

If another single-differenced high-low phase measurement can be obtained between i-th ground receiver, k-th GPS satellite, and the user satellite, a double-differenced high-low phase measurement can be formed by subtracting those two single-differenced high-low phase measurements.

$$DDHLP^c{}_{iu}^{jk} = -f^j \cdot \left[\delta t_{ci} + \rho_i{}^j(t_{Ri})/c + \delta t_{\phi_i}{}^j \right]$$

$$+ f^j \cdot [\; \delta t_{c_u} + \rho_u{}^j(t_{R_u})/c + \delta t_{\phi_u}{}^j \;]$$

$$+ f^k \cdot [\; \delta t_{c_i} + \rho_i{}^k(t_{R_i})/c + \delta t_{\phi_i}{}^k \;]$$

$$- f^k \cdot [\ \delta t_{c_u} + \rho_u{}^k(t_{R_u})/c + \delta t_{\phi_u}{}^k\ ]$$

$$+\ \phi^j(t_i)\ -\ \phi^k(t_i)\ -\ \phi^j(t_u)\ +\ \phi^k(t_u)$$

$$+N_{iu}^{jk} \tag{4.2.14}$$

where $N_{iu}^{jk} = N_i^j(t_{0i}) - N_u^j(t_{0u}) - N_i^k(t_{0i}) + N_u^k(t_{0u})$. In Eq. (4.2.14), all the phase terms associated with the ground station and user satellite receivers are canceled out.

By multiplying a negative nominal wave length, $-\lambda = -c/f_0$, Eq. (4.2.14) becomes the double-differenced high-low phase pseudorange measurement,

$$
DDHL_{iu}^{c\,jk} = \left(\frac{f^j}{f_0}\right) \cdot \left(\rho_i^j(t_{R_i}) - \rho_u^j(t_{R_u})\right) - \left(\frac{f^k}{f_0}\right) \cdot \left(\rho_i^k(t_{R_i}) - \rho_u^k(t_{R_u})\right)
$$

$$
-\left(\frac{c}{f_0}\right) \cdot \left(\phi^j(t_i) - \phi^k(t_i) - \phi^j(t_u) + \phi^k(t_u)\right)
$$

$$
+\ c \cdot \left(\frac{f^j - f^k}{f_0}\right) \cdot (\delta t_{c_i} - \delta t_{c_u})
$$

$$
+\ \left(\frac{f^j}{f_0}\right) \cdot (\delta \rho_{\phi_i}^j - \delta \rho_{\phi_u}^j)\ -\ \left(\frac{f^k}{f_0}\right) \cdot (\delta \rho_{\phi_i}^k - \delta \rho_{\phi_u}^k)
$$

$$
+\ C_{iu}^{jk} \tag{4.2.15}
$$

where $\delta \rho_\phi = -c \cdot \delta t_\phi$, and $C_{iu}^{jk} = -\lambda \cdot N_{iu}^{jk}$. Note that Eq. (4.2.15) contains two different time tags, t_i and t_u. If the ground station receiver clock and the on-board receiver clock are synchronized, then the second line can be canceled out. Since both the ICESat/GLAS on-board receiver clock and the ground station receiver clock will

be synchronized within 1 microsecond with the GPS System Time, the second line can be canceled out.

Since the GPS satellites have highly stable oscillators, which have 10^{-11} or 10^{-12} clock drift rate, the frequencies of those clocks usually stay close to the nominal frequency, f_0. If the frequencies are expressed as $f^j = f_0 + \Delta f^j$ and $f^k = f_0 + \Delta f^k$, Eq. (4.2.15) becomes

$$
\begin{aligned}
DDHL^{c\,jk}_{iu} = &\; \rho_i^j(t_{R_i}) - \rho_u^j(t_{R_u}) - \rho_i^k(t_{R_i}) + \rho_u^k(t_{R_u}) \\
&+ \left(\frac{\Delta f^j}{f_0}\right) \cdot (\rho_i^j(t_{R_i}) - \rho_u^j(t_{R_u})) \; - \; \left(\frac{\Delta f^k}{f_0}\right) \cdot (\rho_i^k(t_{R_i}) - \rho_u^k(t_{R_u})) \\
&+ \; c \cdot \left(\frac{\Delta f^j - \Delta f^k}{f_0}\right) \cdot (\delta t_{c_i} - \delta t_{c_u}) \\
&+ \; \delta\rho_{\phi i}^{\;j} - \delta\rho_{\phi u}^{\;j} - \delta\rho_{\phi i}^{\;k} + \delta\rho_{\phi u}^{\;k} \\
&+ \left(\frac{\Delta f^j}{f_0}\right) \cdot (\delta\rho_{\phi i}^{\;j} - \delta\rho_{\phi u}^{\;j}) \; - \; \left(\frac{\Delta f^k}{f_0}\right) \cdot (\delta\rho_{\phi i}^{\;k} - \delta\rho_{\phi u}^{\;k}) \\
&+ \; C^{jk}_{iu}
\end{aligned}
\tag{4.2.16}
$$

For the ICESat/GLAS-GPS case, the single differenced range can be 600 km to 6200 km. If we assume 10^{-11} clock drift rate for GPS satellite clocks, the second line contributes an effect, which is at the sub-millimeter level to the double differenced range measurement. This effect is less than the noise level, and as a consequence, the contribution from the second line can be ignored. Since the performance specification of the time-tag errors of the flight and ground receivers for ICESat/GLAS mission is required to be less than 1 microsecond with respect to the GPS System Time, the third

line also is negligible. The fifth line is totally negligible, because even for the propagation delay of 100 m, the contribution from this line is less than 10^{-9} meters. The first line in Eq. (4.2.16) can be expanded by the linear approximation after substituting Eqs. (4.2.4a) and (4.2.4b), to obtain:

$$DDHL_{iu}^{c\ jk} = \rho_i^j(t_i) - \rho_u^j(t_u) - \rho_i^k(t_i) + \rho_u^k(t_u)$$

$$- \left[\dot{\rho}_i^j(t_i) - \dot{\rho}_i^k(t_i)\right] \cdot \ \delta t_{c_i} + \left[\dot{\rho}_u^j(t_u) - \dot{\rho}_u^k(t_u)\right] \cdot \ \delta t_{c_u}$$

$$+ \ \delta\rho_{\phi_i}^j - \delta\rho_{\phi_u}^j - \delta\rho_{\phi_i}^k + \delta\rho_{\phi_u}^k$$

$$+ \ C_{iu}^{jk} \tag{4.2.17}$$

This equation is implemented for the double-differenced high-low phase pseudorange measurement. The second line does not need to be computed if the ground stations and the ICESat/GLAS on-board receiver's time-tags are corrected in the preprocessing stage by using independent clock information from the pseudo-range measurement. If such clock information is not available, then the receiver clock errors, δt_{c_i} and δt_{c_u}, can be modeled as linear functions,

$$\delta t_{c_i} = a_i + b_i (t_i - t_{i0}) \tag{4.2.18a}$$

$$\delta t_{c_u} = a_u + b_u (t_u - t_{u0}) \tag{4.2.18b}$$

where (a_i, b_i) and (a_u, b_u) are pairs of clock bias and clock drift for i-th ground station receiver clock and the user satellite clock, respectively, and t_{i0} and t_{u0} are the reference time for clock parameters for i-th ground station receiver clock and the user satellite clock.

The third line of Eq. (4.2.17) includes the propagation delay and the relativistic effects for the high-low phase converted measurement. These effects are discussed in more detail in the following sections.

4.2.4   Corrections

4.2.4.1   Propagation Delay

When a radio wave is traveling through the atmosphere of the Earth, it experiences a delay due to the propagation refraction. Atmospheric scientists usually divide the atmosphere into four layers: the troposphere, the stratosphere, the mesosphere, and the thermosphere. The troposphere, the lowest layer of the Earth's atmosphere, contains 99% of the atmosphere's water vapor and 90% of the air mass. The tropospheric bending is therefore treated using both dry and wet components. The dry path delay is caused by the atmosphere gas content along the propagated path through the troposphere while the wet path delay is caused by the water vapor content along the same path. Since the tropospheric path delay of a radio wave is frequency independent, this path delay cannot be isolated using multiple frequencies. The tropospheric path delays caused by the dry portion, which accounts for 80% or more of the delay, can be modeled with an accuracy of two to five percent for L-band frequencies [*Atlshuler & Kalaghan*, 1974]. Although the contribution from the wet component is relatively small, it is more difficult to model because surface measurements of water vapor cannot be applied to completely describe the regional variations in the water vapor distribution, especially with respect to horizontal

variation, of the water vapor field. There are several approaches to model the wet component of the tropospheric path delay. One approach is to use one of the empirical atmospheric models based on the measurement of meteorological parameters at the Earth's surface or the altitude profile with radisondes and apply regional modeling. The other approach is to map the water vapor content in various directions directly using devices like water vapor radiometer (WVR). List of references for these approaches can be found in *Tralli et al.* [1988]. A third approach is to solve for tropospheric path delay parameters. Chao's model [*Chao*, 1974], modified Hopfield model [*Goad and Goodman*, 1974; *Remondi*, 1984], or MTT model [*Herring*, 1992] are among several candidates which can be implemented for the tropospheric correction.

The ionosphere is a region of the Earth's upper atmosphere, approximately 100 km to 1000 km above the Earth's surface, where electrons and ions are present in quantities sufficient to affect the propagation of radio waves. The path delay will be proportional to the number of electrons along the slant path between the satellite and the receiver, and the electron density distribution varies with altitude, time of day time of year, solar and geomagnetic activity, and the time within the solar sunspot cycle. The ionospheric path delay depends on the frequency of the radio signal. The ionospheric bending on L1 GPS measurement will vary from about 0.15 m to 50 m [*Clynch and Coco*, 1986]. Some of this delay can be eliminated by ionospheric modeling [for example, *Finn and Matthewman*, 1989]. However, more accurate corrections can be made by using the dual frequency measurements routinely acquired by the GPS receivers. The correction method for the dual frequency GPS

measurements can be found in Section 6.5.2. *Hofmann-Wellenhof et al.* [1992] provides more detailed description of the propagation delay for GPS measurements.

4.2.4.2   Relativistic Effect

The relativistic effects on GPS measurements can be summarized as follows. Due to the difference in the gravitational potential, the satellite clock tends to run faster than the ground station's [*Spilker*, 1978; *Gibson*, 1983]. These effects can be divided into two parts: a constant drift and a periodic effect. The constant drift can be removed by off-setting the GPS clock frequency low before launch to account for that constant drift. The periodic relativistic effects can be modeled for a high-low measurement as

$$\Delta\rho_{srel} = \frac{2}{c}(\bar{r}_l \cdot \bar{v}_l - \bar{r}_h \cdot \bar{v}_h) \qquad (4.2.20)$$

where

$\Delta\rho_{srel}$ $\quad$ = correction for the special relativity

c $\qquad\quad$ = speed of light

$\bar{r}_l, \bar{v}_l$ $\qquad$ = the position and velocity of the low satellite or tracking stations

$\bar{r}_h, \bar{v}_h$ $\qquad$ = the position and velocity of the high satellite

The coordinate speed of light is reduced when light passes near a massive body causing a time delay, which can be modeled as [*Holdridge*, 1967]

$$\Delta\rho_{grel} = (1 + \gamma)\frac{GM_e}{c^2}\ln\left(\frac{r_{tr} + r_{rec} + \rho}{r_{tr} + r_{rec} - \rho}\right) \qquad (4.2.21)$$

where

$\Delta\rho_{grel}$ $\quad$ = correction for the general relativity

γ = the parameterized post-Newtonian (PPN) parameter ($\gamma = 1$ for general relativity)

GM_e = gravitational constant for the Earth

ρ = the relativistically uncorrected range between the transmitter and the receiver

r_{tr} = the geocentric radial distance of the transmitter

r_{rec} = the geocentric radial distance of the receiver

4.2.4.3   Phase Center Offset

The geometric offset between the transmitter and receiver phase centers and the effective satellite body-fixed reference point can be modeled depending on the satellite orientation (attitude) and spacecraft geometry. The ICESat/GLAS antenna location will be known and implemented when the fabrication of the satellite is complete. However, the location of the antenna phase center with respect to the spacecraft center of mass will also be required.   This position vector will be essentially constant in spacecraft fixed axes, but this correction is necessary since the equations of motion refer to the spacecraft center of mass.

4.2.4.4   Ground Station Related Effects

In computing the double-differenced phase-converted high-low pseudo-range measurement, it is necessary to consider the effects of the displacement of the ground station location caused by the crustal motions. Among these effects, tidal effects and tectonic plate motion effects are most prominent.

Station displacements arising from tidal effects can be divided into three parts,

$$\Delta_{tide} = \Delta_{dtide} + \Delta_{ocean} + \Delta_{rotate} \tag{4.2.22}$$

where

Δ_{tide} = the total displacement due to the tidal effects

Δ_{dtide} = the displacement due to the solid Earth tide

Δ_{ocean} = the displacement due to the ocean loading

Δ_{rotate} = the displacement due to the rotational deformation

The approach of the IERS Conventions [*McCarthy,* 1996] have been implemented for the solid Earth tide correction. Ocean loading effects are due to the elastic response of the Earth's crust to loading induced by the ocean tides. The displacement due to the rotational deformation is the displacement of the ground station by the elastic response of the Earth's crust to shifts in the spin axis orientation [*Goad*, 1980] which occur at both tidal and non-tidal periods. Detailed models for the effects of solid Earth tide, the ocean loading, and the rotational deformation, can be found in *Yuan* [1991].

The effect of the tectonic plate motion, which is based on the relative plate motion model AM0-2 of *Minster and Jordan* [1978], is modeled as

$$\overline{\Delta}_{tect} = (\overline{\omega}_p \times \overline{R}_{s_0})(t_i - t_0) \tag{4.2.23}$$

where

$\overline{\Delta}_{tect}$ = the displacement due to the tectonic motion

$\overline{\omega}_p$ = the angular velocity of the tectonic plate

$\overline{R}_{s_0}$ = the Earth-fixed coordinates of the station at t_i

$$t_0 \qquad = \text{ a reference epoch}$$

4.2.5   *Measurement Model Partial Derivatives*

The partial derivatives of Eq. (4.2.18) with respect to various model parameters are given in this section. The considered parameters include the ground station positions, GPS satellite's positions, ICESat's positions, clock parameters, ambiguity parameters, and tropospheric refraction parameters.

The partial derivatives of Eq. (4.2.18) with respect to the *i*-th ground station positions, (x_{1i}, x_{2i}, x_{3i}), are

$$\frac{\partial DDHL^{c\,jk}_{iu}}{\partial x_{mi}} = \frac{(x_{mi} - x_m{}^j)}{\rho_i^j} - \frac{(x_{mi} - x_m{}^k)}{\rho_i^k}, \qquad \text{for } m=1,2,3 \qquad (4.2.24)$$

where ρ_i^j is the range between *i*-th ground station receiver and *j*-th transmitter, and ρ_i^k is the range between *i*-th ground station receiver and *k*-th transmitter such that

$$\rho_i^j = \sqrt{(x_{1i} - x_1^j)^2 + (x_{2i} - x_2^j)^2 + (x_{3i} - x_3^j)^2} \qquad (4.2.25)$$

$$\rho_i^k = \sqrt{(x_{1i} - x_1^k)^2 + (x_{2i} - x_2^k)^2 + (x_{3i} - x_3^k)^2} \qquad (4.2.26)$$

and (x_1^j, x_2^j, x_3^j) and (x_1^k, x_2^k, x_3^k) are the *j*-th and *k*-th transmitter Cartesian positions, respectively.

The partial derivatives of Eq. (4.2.18) with respect to the *j*-th and *k*-th transmitter positions are

$$\frac{\partial DDHL_{iu}^{c\,jk}}{\partial x_m^{\,j}} = \frac{(x_{mi} - x_m^{\,j})}{\rho_i^{\,j}} + \frac{(x_{mu} - x_m^{\,j})}{\rho_u^{\,j}}, \qquad \text{for } m=1,2,3 \qquad (4.2.27)$$

$$\frac{\partial DDHL_{iu}^{c\,jk}}{\partial x_m^{\,k}} = \frac{(x_{mi} - x_m^{\,k})}{\rho_i^{\,k}} - \frac{(x_{mu} - x_m^{\,k})}{\rho_u^{\,k}}, \qquad \text{for } m=1,2,3 \qquad (4.2.28)$$

where $\rho_u^{\,j}$ is the range between j-th transmitter and the user satellite, and $\rho_u^{\,k}$ is the range between k-th transmitter and the user satellite such that

$$\rho_u^{\,j} = \sqrt{(x_{1u} - x_1^{\,j})^2 + (x_{2u} - x_2^{\,j})^2 + (x_{3u} - x_3^{\,j})^2} \qquad (4.2.29)$$

$$\rho_u^{\,k} = \sqrt{(x_{1u} - x_1^{\,k})^2 + (x_{2u} - x_2^{\,k})^2 + (x_{3u} - x_3^{\,k})^2} \qquad (4.2.30)$$

and (x_{1u}, x_{2u}, x_{3u}) are the user satellite's Cartesian positions.

The partial derivatives of Eq. (4.2.18) with respect to the user satellite positions are

$$\frac{\partial DDHL_{iu}^{c\,jk}}{\partial x_{mu}} = -\frac{(x_{mu} - x_m^{\,j})}{\rho_u^{\,j}} + \frac{(x_{mu} - x_m^{\,k})}{\rho_u^{\,k}}, \qquad \text{for } m=1,2,3 \qquad (4.2.31)$$

The partial derivatives of Eq. (4.2.18) with respect to the clock parameters of Eqs. (4.2.19a) and (4.2.19b) are

$$\frac{\partial DDHL_{iu}^{c\,jk}}{\partial a_i} = -(\dot{\rho}_i^{\,j} - \dot{\rho}_i^{\,k}) \qquad (4.2.32)$$

$$\frac{\partial DDHL_{iu}^{c\,jk}}{\partial b_i} = -(\dot{\rho}_i^{\,j} - \dot{\rho}_i^{\,k}) \cdot (t_i - t_{i0}) \qquad (4.2.33)$$

and

$$\frac{\partial DDHL_{iu}^{c\,jk}}{\partial a_u} = (\dot{\rho}_u^{\,j} - \dot{\rho}_u^{\,k}) \tag{4.2.34}$$

$$\frac{\partial DDHL_{iu}^{c\,jk}}{\partial b_u} = (\dot{\rho}_u^{\,j} - \dot{\rho}_u^{\,k}) \cdot (t_u - t_{u0}) \tag{4.2.35}$$

The partial derivative of Eq. (4.2.18) for the double-differenced ambiguity parameter, C_{iu}^{jk}, is

$$\frac{\partial DDHL_{iu}^{c\,jk}}{\partial C_{iu}^{jk}} = 1 \tag{4.2.36}$$

When Chao's model is used, the partial derivative of Eq. (4.2.18) with respect to the i-th ground station's zenith delay parameter, Z_i, is

$$\frac{\partial DDHL_{iu}^{c\,jk}}{\partial Z_i} = \left(\frac{1}{\sin E_i^{\,j} + \dfrac{0.00143}{\tan E_i^{\,j} + 0.0445}} + \frac{1}{\sin E_i^{\,j} + \dfrac{0.00035}{\tan E_i^{\,j} + 0.017}} \right)$$

$$- \left(\frac{1}{\sin E_i^{\,k} + \dfrac{0.00143}{\tan E_i^{\,k} + 0.0445}} + \frac{1}{\sin E_i^{\,k} + \dfrac{0.00035}{\tan E_i^{\,k} + 0.017}} \right)$$

$$\tag{4.2.37}$$

where $E_i^{\,j}$ and $E_i^{\,k}$ are the elevation angles of the j-th and k-th GPS satellite transmitters from i-th ground station, respectively.

4.3   SLR Measurement Model

4.3.1   Range Model and Corrections

Laser tracking instruments record the travel time of a short laser pulse from the reference point (opticalaxis) to the satellite retroreflector and back. The one-way range from the reference point of the ranging instrument to the retroreflector of the satellite, ρ^o, can be expressed in terms of the round trip light time, $\Delta\tau$ as

$$\rho^o = \frac{1}{2}c\Delta\tau + \varepsilon \qquad (4.3.1)$$

where

    c = the speed of light

    ε = measurement error.

The computed one-way signal path between the reference point on the satellite and the ground station, ρ^c, can be expressed as

$$\rho^c = |\bar{r} - \bar{r}_s| + \Delta\rho_{trop} + \Delta\rho_{grel} + \Delta\rho_{c.m.} \qquad (4.3.2)$$

where

    $\bar{r}$ = the satellite position in geocentric coordinates

    $\bar{r}_s$ = the position of the tracking station in geocentric coordinates

    $\Delta\rho_{trop}$ = correction for tropospheric delay

    $\Delta\rho_{grel}$ = correction for the general relativity

    $\Delta\rho_{c.m.}$ = correction for the offset of the satellite's center-of-mass and the

                         laser retroreflector

The tropospheric refraction correction is computed using the model of *Marini and Murray* [1973]. The correction for the general relativity in SLR measurements is the

same as for GPS measurement, which is expressed in Eq. (4.2.21). The effects of the displacement of the ground station location caused by the crustral motions should be considered. These crustal motions include tidal effects and tectonic plate motion effects, which are described in Eqs. (4.2.22) and (4.2.23), respectively.

4.3.2   Measurement Model Partial Derivatives

The partial derivatives of Eq. (4.3.2) with respect to various model parameters are derived in this section. The considered parameters include the ground station positions, satellite's positions.

The partial derivatives of Eq. (4.3.2) with respect to the ground station positions, (r_{s1}, r_{s2}, r_{s3}), are

$$\frac{\partial \rho^c}{\partial r_{si}} = \frac{(r_{si} - r_i)}{\rho}, \qquad \text{for } i=1,2,3 \qquad (4.3.3)$$

where (r_1, r_2, r_3) are the satellite's positions, and ρ is the range between the ground station and the satellite such that

$$\rho = \sqrt{(r_1 - r_{s1})^2 + (r_2 - r_{s2})^2 + (r_3 - r_{s3})^2} \qquad (4.3.4)$$

The partial derivatives of Eq. (4.3.2) with respect to the satellite's positions, (r_1, r_2, r_3), are

$$\frac{\partial \rho^c}{\partial r_i} = \frac{(r_i - r_{si})}{\rho}, \qquad \text{for } i=1,2,3 \qquad (4.3.5)$$

5.0   ALGORITHM DESCRIPTION: Estimation

A least squares batch filter [*Tapley*, 1973] is our adopted approach for the estimation procedure.   Since multi-satellite orbit determination problems require extensive usage of computer memory for computation, it is essential to consider the computational efficiency in the problem formulation.   This section describes the estimation procedures for ICESat/GLAS POD, including the problem formulation for multi-satellite orbit determination.

5.1   Least Squares Estimation

The equations of motion for the satellite can be expressed as

$$\dot{X}(t) \ = \ F(X,t), \qquad\qquad X(t_0) \ = \ X_0 \qquad\qquad (5.1.1)$$

where X is the n-dimensional state vector, F is a non-linear n-dimensional vector function of the state, and X_0 is the value of the state at the initial time t_0, which is not known perfectly.   The tracking observations can be expressed as discrete measurements of quantities, which are a function of the state. Thus the observation-state relationship can be written as

$$Y_i = G(X_i, t_i) + \varepsilon_i \qquad\qquad i = 1, \cdots, l \qquad\qquad (5.1.2)$$

where Y_i is a p vector of the observations made at time t_i, (X_i, t_i) is a non-linear vector function relating the state to the observations, and ε_i is the measurement noise.

If a reference trajectory is available and if X, the true trajectory, and X^*, the reference trajectory, remain sufficiently close throughout the time interval of interest, the trajectory for the actual motion can be expanded in a Taylor series about

the reference trajectory to obtain a set of differential equations with time dependent coefficients. Using a similar procedure to expand the nonlinear observation-state relation, a linear relation between the observation deviation and the state deviation can be obtained. Then, the nonlinear orbit determination problem can be replaced by a linear orbit determination problem in which the deviation from the reference trajectory is to be determined. In practice, this linearization of the problem requires an iterative adjustment which yields successively smaller adjustments to the state parameters to optimally fit the observations.

Let

$$x(t) = X(t) - X^*(t) \qquad y(t) = Y(t) - Y^*(t) \tag{5.1.3}$$

where $X^*(t)$ is a specified reference trajectory and $Y^*(t)$ is the value of the observation calculated by using $X^*(t)$. Then, substituting Eq. (5.1.3) into Eqs. (5.1.1) and (5.1.2), expanding in a Taylor's series, and neglecting higher order terms leads to the relations

$$\dot{x} = A(t)x, \qquad x(t_0) = x_0$$

$$y_i = \widetilde{H}_i x_i + \varepsilon_i \qquad i = 1, \cdots, l \tag{5.1.4}$$

where

$$A(t) = \frac{\partial F}{\partial X}(X^*, t) \qquad \widetilde{H} = \frac{\partial G}{\partial X}(X^*, t) \tag{5.1.5}$$

The general solution to Eq. (5.1.4) can be expressed as

$$x(t) = \Phi(t, t_0)x_0 \tag{5.1.6}$$

where the state transition matrix $\Phi(t, t_0)$ satisfies the differential equation:

$$\dot{\Phi}(t,t_0) \;=\; A(t)\Phi(t,t_0), \qquad\qquad \Phi(t_0,t_0) \;=\; I \qquad\qquad (5.1.7)$$

where I is the $n \times n$ identity matrix.

Using Eq. (5.1.5), the second of Eq. (5.1.3) may be written in terms of the state at t_0 as

$$y_i = \widetilde{H}_i \Phi(t_i,t_0)x_0 + \varepsilon_i, \qquad\qquad i = 1, \cdots, l \qquad\qquad (5.1.8)$$

Using the solution for the linearized state equation (Eq. (5.1.6)), Eq. (5.1.8) may be rewritten as

$$y = Hx_0 + \varepsilon \qquad\qquad (5.1.9)$$

where

$$y = \begin{bmatrix} y_1 \\ \vdots \\ y_l \end{bmatrix} \qquad H = \begin{bmatrix} \widetilde{H}_1 \Phi(t_1,t_0) \\ \vdots \\ \widetilde{H}_l \Phi(t_l,t_0) \end{bmatrix} \qquad \varepsilon = \begin{bmatrix} \varepsilon_1 \\ \vdots \\ \varepsilon_l \end{bmatrix} \qquad (5.1.10)$$

where y and ε are m vectors ($m = l \times p$) and H is an $m \times n$ matrix. Equation (5.1.9) is a system of m equations in n unknowns. In practical orbit determination problems, there are more observations than estimated parameters ($m > n$), which means that Eq. (5.1.9) is overdetermined. It is usually assumed that the observation error vector, ε, satisfies the a priori statistics, $E[\varepsilon] = 0$ and $E[\varepsilon\varepsilon^T] = W^{-1}$. By scaling each term in Eq. (5.1.9) by $W^{1/2}$, the condition

$$W^{1/2}[\varepsilon\varepsilon^T]W^{T/2} = W^{1/2}W^{-1}W^{T/2} = I \qquad\qquad (5.1.11)$$

is obtained.

An approach to obtain the best estimate of $\hat{x}$, given the linear observation-state relations (Eq. (5.1.9)) is described in the following discussions. The method obtains the solution by applying successive orthogonal transformations to the linear equations given in Eq. (5.1.9). Consider the quadratic performance index

$$J = \frac{1}{2} \| W^{1/2}(Hx - y) \|^2 = \frac{1}{2}(Hx - y)^T W(Hx - y) \tag{5.1.12}$$

The solution to the weighted least-squares estimation problem (which is equivalent to the minimum variance and the maximum likelihood estimation problem, under certain restrictions) is obtained by finding the value $\hat{x}$ which minimizes Eq. (5.1.12). To achieve the minimum value of Eq. (5.1.12) let Q be an m×m orthogonal matrix. Hence, it follows that Eq. (5.1.12) can be expressed as

$$J = \frac{1}{2} \| QW^{1/2}(Hx - y) \|^2 \tag{5.1.13}$$

Now, if Q is selected such that

$$QW^{1/2}H = \begin{bmatrix} R \\ 0 \end{bmatrix} \qquad QW^{1/2}y = \begin{bmatrix} b \\ e \end{bmatrix} \tag{5.1.14}$$

where R is $n \times n$ upper-triangular, 0 is an $(m-n) \times n$ null matrix, b is $n \times 1$ vector, and e is an $(m-n) \times 1$ vector. Equation (5.1.13) can be written then as

$$J(x) = \frac{1}{2} \| Rx - b \|^2 + \frac{1}{2} \| e \|^2 \tag{5.1.15}$$

The value of x, which minimizes Eq. (5.1.12), is obtained by the solution

$$R\hat{x} = b \tag{5.1.16}$$

and the minimum value of the performance index becomes

$$J(\hat{x}) = \frac{1}{2} \| e \|^2 = \frac{1}{2} \| y - H\hat{x} \|^2 \tag{5.1.17}$$

That is, e provides an estimate of the residual error vector.

The procedures is direct and for implementation requires only that a convenient computational procedure for computing $QW^{1/2}H$ and $QW^{1/2}y$ be available. The two most frequently applied methods are the Givens method, based on a sequence of orthogonal rotations, and the Householder method, based on a series of orthogonal reflections [*Lawson and Hanson*, 1974].

In addition to the expression for computing the estimate, the statistical properties of the error in the estimate, R, are required. If the error in the estimate, η, is defined as

$$\eta = \widehat{x} - x \tag{5.1.18}$$

it follows that

$$E[\eta] = E[\hat{x} - x] = E[R^{-1}b - x] \tag{5.1.19}$$

Since

$$QW^{1/2}y = QW^{1/2}Hx + QW^{1/2}\varepsilon$$

leads to

$$b = Rx + \widetilde{\varepsilon} \tag{5.1.20}$$

it follows that

$$E[\eta] = E[R^{-1}(Rx + \widetilde{\varepsilon}) - x] = E[R^{-1}\widetilde{\varepsilon}] \tag{5.1.21}$$

As noted in Eq. (5.1.11), if the observation error, ε, is unbiased, $\widetilde{\varepsilon} = QW^{1/2}\varepsilon$ will be unbiased and

$$E[\eta] = 0 \tag{5.1.22}$$

Hence, $\hat{x}$ will be an unbiased estimate of x. Similarly, the covariance matrix for the error in x can be expressed as

$$P = E[\eta\eta^T]$$

$$= E[R^{-1}\widetilde{\varepsilon\varepsilon}^T R^{-T}] = R^{-1}E[\widetilde{\varepsilon\varepsilon}^T]R^{-T} \tag{5.1.23}$$

If the observation error, ε, has a statistical covariance defined as $E[\varepsilon\varepsilon^T] = W^{-1}$, the estimation error covariance matrix is given by $E[\widetilde{\varepsilon\varepsilon}^T] = W^{1/2}E[\varepsilon\varepsilon^T]W^{T/2} = W^{1/2}W^{-1}W^{T/2} = I$. Consequently, relation (5.1.23) leads to

$$P = R^{-1}R^{-T} \tag{5.1.24}$$

It follows then that the estimate of the state and the associated error covariance matrix are given by the expressions

$$\hat{x} = R^{-1}b \tag{5.1.25}$$

$$P = R^{-1}R^{-T} \tag{5.1.26}$$

5.2   Problem Formulation for Multi-Satellite Orbit Determination

Proper categorization of the parameters will help to clarify the problem formulation. Parameters can be divided into two groups: dynamic parameters and kinematic parameters. Dynamic parameters need to be mapped into other states by using the state transition matrix, which is usually computed by numerical integration, while kinematic parameters are treated as constant throughout the computation. Dynamic parameters can be grouped again into two parts as the local dynamic

parameters and global dynamic parameters. Local dynamic parameters are satellite-specific. Global dynamic parameters are parameters, which influence every satellite, such as those defining gravitational forces.

Following the categorization described above, the estimation state vector is defined as

$$X \equiv \begin{bmatrix} X_{KP} \\ X_{SS} \\ X_{LDP} \\ X_{GDP} \end{bmatrix} \tag{5.2.1}$$

where

X_{KP} = the kinematic parameters (n_{kp})

X_{SS} = the satellite states (n_{ss})

X_{LDP} = the local dynamic parameters (n_{ldp})

X_{GDP} = the global dynamic parameters (n_{gdp})

and X_{SS} consists of satellites' positions and velocities, i.e. $X_{SS} \equiv [X_{POS}, X_{VEL}]^T$. For ns-satellites, where ns is the total number of satellites which will be estimated, X_{SS} becomes

$$X_{SS} = \begin{bmatrix} \bar{r}_1 \\ \bar{r}_2 \\ \vdots \\ \bar{r}_{ns} \\ \hline \bar{v}_1 \\ \bar{v}_2 \\ \vdots \\ \bar{v}_{ns} \end{bmatrix}$$

where $\bar{r}_i$ and $\bar{v}_i$ are the 3×1 position and velocity vectors of the i-th satellite, respectively.

The differential equations of state, Eq. (5.1.1), becomes

$$\dot{X}(t) = F(X,t) = \begin{bmatrix} 0 \\ \dot{X}_{SS} \\ 0 \\ 0 \end{bmatrix}, \qquad X(t_0) = X_0 \qquad (5.2.2)$$

where

$$\dot{X}_{SS} = \begin{bmatrix} \bar{v}_1 \\ \bar{v}_2 \\ \vdots \\ \bar{v}_{ns} \\ \hline \bar{f}_1 \\ \bar{f}_2 \\ \vdots \\ \bar{f}_{ns} \end{bmatrix} \qquad (5.2.3)$$

and $\bar{f}_i = \bar{a}_{g_i} + \bar{a}_{ng_i}$ for i-th satellite. Eq. (5.2.2) represent a system of n nonlinear first order differential equations which includes $n_{ss} = 6 \times ns$ of Eq. (5.2.3). After the linearization process described in section 5.1, Eq. (5.2.2) becomes Eqs. (5.1.6) and (5.1.7).

Since Eq. (5.1.7) represents n^2 coupled first order ordinary differential equations, the dimension of the integration vector becomes $n_{ss} + n^2$. However, $A(t)$ matrix is a sparse matrix, because of the nature of the parameters. And $A(t)$ matrix becomes even sparser, since each satellite's state is independent of the others, i.e. $(\bar{r}_i, \bar{v}_i)$ is independent of $(\bar{r}_j, \bar{v}_j)$ for $i \neq j$. Using the partitioning of Eq. (5.2.1), $A(t)$ becomes

$$A = \begin{bmatrix} 0 & 0 & 0 & 0 & 0 \\ 0 & 0 & I & 0 & 0 \\ 0 & A_{32} & A_{33} & A_{34} & A_{35} \\ 0 & 0 & 0 & 0 & 0 \\ 0 & 0 & 0 & 0 & 0 \end{bmatrix} \qquad (5.2.4)$$

where

$$A_{32} = \begin{bmatrix} \dfrac{\partial \bar{f}_1}{\partial \bar{r}_1} & \cdots 0 \cdots & \cdots 0 \\ \vdots & & \vdots \\ 0 & \ddots & 0 \\ \vdots & & \vdots \\ 0 & \cdots 0 \cdots & \dfrac{\partial \bar{f}_{ns}}{\partial \bar{r}_{ns}} \end{bmatrix} \qquad A_{33} = \begin{bmatrix} \dfrac{\partial \bar{f}_1}{\partial \bar{v}_1} & \cdots 0 \cdots & \cdots 0 \\ \vdots & & \vdots \\ 0 & \ddots & 0 \\ \vdots & & \vdots \\ 0 & \cdots 0 \cdots & \dfrac{\partial \bar{f}_{ns}}{\partial \bar{v}_{ns}} \end{bmatrix}$$

$$A_{34} = \begin{bmatrix} \dfrac{\partial \bar{f}_1}{\partial X_{LDP_1}} & \cdots 0 \cdots & \cdots 0 \\ \vdots & & \vdots \\ 0 & \ddots & 0 \\ \vdots & & \vdots \\ 0 & \cdots 0 \cdots & \dfrac{\partial \bar{f}_{ns}}{\partial X_{LDP_{ns}}} \end{bmatrix} \qquad A_{35} = \begin{bmatrix} \dfrac{\partial \bar{f}_1}{\partial X_{GDP_1}} \\ \vdots \\ \dfrac{\partial \bar{f}_{ns}}{\partial X_{GDP_{ns}}} \end{bmatrix}$$

Note that A_{32}, A_{33}, and A_{34} are all block diagonal matrix, and A_{33} would be zero if the perturbations do not depend on satellites' velocity. Atmospheric drag is one example of perturbations, which depend on the satellite's velocity.

If $\Phi = \begin{bmatrix} \phi_{ij} \end{bmatrix}$, for $i, j = 1, \cdots, 5$, Eq. (5.1.7) becomes

$$\dot{\Phi} = \begin{bmatrix} 0 & 0 & 0 & 0 & 0 \\ \phi_{31} & \phi_{32} & \phi_{33} & \phi_{34} & \phi_{35} \\ B_{11} & B_{12} & B_{13} & B_{14} & B_{15} \\ 0 & 0 & 0 & 0 & 0 \\ 0 & 0 & 0 & 0 & 0 \end{bmatrix} \qquad (5.2.5)$$

where $\quad B_{1j} = A_{32}\phi_{2j} + A_{33}\phi_{3j} + A_{34}\phi_{4j} + A_{35}\phi_{5j} \quad$ for $j = 1, \cdots, 5.$

Integrating the first row and last two rows of Eq. (5.2.4) with the initial conditions, $\quad \Phi(t_0,t_0) = I \quad$ yields the results that $\phi_{11}=\phi_{44}=\phi_{55}=I$ and $\phi_{12}=\phi_{13}=\phi_{14}=\phi_{15}=\phi_{41}=\phi_{42}=\phi_{43}=\phi_{45}=\phi_{51}=\phi_{52}=\phi_{53}=\phi_{54}=0.$ After substituting these results to $B_{1j}, j=1,\cdots,5$, we have

$$B_{11} = A_{32}\phi_{21} + A_{33}\phi_{31}$$

$$B_{12} = A_{32}\phi_{22} + A_{33}\phi_{32}$$

$$B_{13} = A_{32}\phi_{23} + A_{33}\phi_{33} \qquad\qquad\qquad (5.2.6)$$

$$B_{14} = A_{32}\phi_{24} + A_{33}\phi_{34} + A_{34}$$

$$B_{15} = A_{32}\phi_{25} + A_{33}\phi_{35} + A_{35}$$

From Eq. (5.2.5) and Eq. (5.2.6), we have

$$\dot{\phi}_{21} = \phi_{31} \qquad\qquad\qquad\qquad (5.2.7a)$$

$$\dot{\phi}_{22} = \phi_{32} \qquad\qquad\qquad\qquad (5.2.8a)$$

$$\dot{\phi}_{23} = \phi_{33} \qquad\qquad\qquad\qquad (5.2.9a)$$

$$\dot{\phi}_{24} = \phi_{34} \qquad\qquad\qquad\qquad (5.2.10a)$$

$$\dot{\phi}_{25} = \phi_{35} \qquad\qquad\qquad\qquad (5.2.11a)$$

$$\dot{\phi}_{31} = A_{32}\phi_{21} + A_{33}\phi_{31} \qquad\qquad\qquad (5.2.7\text{b})$$

$$\dot{\phi}_{32} = A_{32}\phi_{22} + A_{33}\phi_{32} \qquad\qquad\qquad (5.2.8\text{b})$$

$$\dot{\phi}_{33} = A_{32}\phi_{23} + A_{33}\phi_{33} \qquad\qquad\qquad (5.2.9\text{b})$$

$$\dot{\phi}_{34} = A_{32}\phi_{24} + A_{33}\phi_{34} + A_{34} \qquad\qquad (5.2.10\text{b})$$

$$\dot{\phi}_{35} = A_{32}\phi_{25} + A_{33}\phi_{35} + A_{35} \qquad\qquad (5.2.11\text{b})$$

From Eqs. (5.2.7a) and (5.2.7b)

$$\ddot{\phi}_{21} \ - \ A_{33}\dot{\phi}_{21} \ - \ A_{32}\phi_{21} \ = \ 0, \qquad \phi_{21}(0) = 0 \quad \dot{\phi}_{21}(0) = 0 \qquad (5.2.12)$$

If we define the partials of accelerations with respect to each group of parameters for the i-th satellite as follows,

$$\frac{\partial \bar{f}_i}{\partial \bar{r}_i} \equiv DADR_i \qquad\qquad\qquad (5.2.13\text{a})$$

$$\frac{\partial \bar{f}_i}{\partial \bar{v}_i} \equiv DADV_i \qquad\qquad\qquad (5.2.13\text{b})$$

$$\frac{\partial \bar{f}_i}{\partial X_{LDP_i}} \equiv DLDP_i \qquad\qquad\qquad (5.2.13\text{c})$$

$$\frac{\partial \bar{f}_i}{\partial X_{GDP_i}} \equiv DGDP_i \qquad\qquad\qquad (5.2.13\text{d})$$

and ϕ_{21} is partitioned as $\phi_{21} = \left[\phi_{21_1}, \cdots, \phi_{21_{ns}}\right]^T$ by $3 \times n_{kp}$ submatrix, ϕ_{21_i}, then, Eq. (5.2.12) become

$$\ddot{\phi}_{21_i} - DADV_i \; \dot{\phi}_{21_i} - DADR_i \; \phi_{21_i} = 0, \qquad i = 1, \cdots, ns \qquad (5.2.14)$$

After applying the initial conditions, $\phi_{21_i}(0) = 0$ and $\dot{\phi}_{21_i}(0) = 0$, to Eq. (5.2.14), we have $\phi_{21} = 0$. And from Eq. (5.2.7a) $\phi_{31} = 0$. From Eqs. (5.2.8a) and (5.2.8b), and Eqs. (5.2.9a) and (5.2.9b), we have similar results as follows.

$$\ddot{\phi}_{22_i} - DADV_i \; \dot{\phi}_{22_i} - DADR_i \; \phi_{22_i} = 0, \qquad i = 1, \cdots, ns \qquad (5.2.15)$$

$$\ddot{\phi}_{23_i} - DADV_i \; \dot{\phi}_{23_i} - DADR_i \; \phi_{23_i} = 0, \qquad i = 1, \cdots, ns \qquad (5.2.16)$$

with the initial conditions $\phi_{22_i}(0) = I$, $\dot{\phi}_{22_i}(0) = 0$, $\phi_{23_i}(0) = 0$, and $\dot{\phi}_{23_i}(0) = I$ for $i = 1, \cdots, ns$.

From Eqs. (5.2.10a) and (5.2.10b), we have

$$\ddot{\phi}_{24} - A_{33}\dot{\phi}_{24} - A_{32}\phi_{24} = A_{34}, \qquad \phi_{24}(0) = 0 \quad \dot{\phi}_{24}(0) = 0 \qquad (5.2.17)$$

If ϕ_{24} is partitioned as $\phi_{24} = \left[\phi_{24_1}, \cdots, \phi_{24_{ns}}\right]^T$ with $3 \times n_{ldp_i}$ submatrix, where n_{ldp_i} is the i-th satellite's number of local dynamic parameters, then it can be shown that all the off-block diagonal terms become zero and the above equation becomes,

$$\ddot{\phi}_{24_i} - DADV_i \; \dot{\phi}_{24_i} - DADR_i \; \phi_{24_i} = DLDP_i, \qquad i = 1, \cdots, ns \qquad (5.2.18)$$

with the initial conditions $\phi_{24_i}(0) = 0$ and $\dot{\phi}_{24_i}(0) = 0$ for $i = 1, \cdots, ns$.

From Eqs. (5.2.11a) and (5.2.11b), we have similar results for ϕ_{25}.

$$\ddot{\phi}_{25_i} - DADV_i\, \dot{\phi}_{25_i} - DADR_i\, \phi_{25_i} = DGDP_i, \qquad i = 1, \cdots, ns \qquad (5.2.19)$$

with the initial conditions $\phi_{25_i}(0) = 0$ and $\dot{\phi}_{25_i}(0) = 0$ for $i = 1, \cdots, ns$.

Combining all these results, we have the state transition matrix for multi-satellite problem as follows:

$$\Phi = \begin{bmatrix} 0 & 0 & 0 & 0 & 0 \\ \phi_{21} & \phi_{22} & \phi_{23} & \phi_{24} & \phi_{25} \\ \dot{\phi}_{21} & \dot{\phi}_{22} & \dot{\phi}_{23} & \dot{\phi}_{24} & \dot{\phi}_{25} \\ 0 & 0 & 0 & 0 & 0 \\ 0 & 0 & 0 & 0 & 0 \end{bmatrix} \qquad (5.2.20)$$

where $\phi_{21} = \dot{\phi}_{21} = 0$ and

$$\phi_{22} = \begin{bmatrix} \phi_{22_1} & & 0 \\ & \ddots & \\ 0 & & \phi_{22_{ns}} \end{bmatrix} \qquad\qquad \phi_{23} = \begin{bmatrix} \phi_{23_1} & & 0 \\ & \ddots & \\ 0 & & \phi_{23_{ns}} \end{bmatrix}$$

$$\phi_{24} = \begin{bmatrix} \phi_{24_1} & & 0 \\ & \ddots & \\ 0 & & \phi_{24_{ns}} \end{bmatrix} \qquad\qquad \phi_{25} = \begin{bmatrix} \phi_{25_1} \\ \vdots \\ \phi_{25_{ns}} \end{bmatrix}$$

By defining $\phi_{\bar{r}_i}$ and $\phi_{\bar{v}_i}$ for i-th satellite as follows,

$$\phi_{\bar{r}_i} \equiv \begin{bmatrix} \phi_{22_i} & \phi_{23_i} & \phi_{24_i} & \phi_{25_i} \end{bmatrix} \qquad (5.2.21a)$$

$$\phi_{\bar{v}_i} \equiv \begin{bmatrix} \dot{\phi}_{22_i} & \dot{\phi}_{23_i} & \dot{\phi}_{24_i} & \dot{\phi}_{25_i} \end{bmatrix} \qquad (5.2.21b)$$

we can compute $\dot{\phi}_{\overline{v}_i} = \begin{bmatrix} \ddot{\phi}_{22_i} & \ddot{\phi}_{23_i} & \ddot{\phi}_{24_i} & \ddot{\phi}_{25_i} \end{bmatrix}$ by substituting Eqs. (5.2.15)-(5.2.16) and Eqs. (5.2.18)-(5.2.19).

$$
\dot{\phi}_{\overline{v}_i} = \begin{bmatrix} DADV_i\ \dot{\phi}_{22_i} + DADR_i\ \phi_{22_i} \\ DADV_i\ \dot{\phi}_{23_i} + DADR_i\ \phi_{23_i} \\ DADV_i\ \dot{\phi}_{24_i} + DADR_i\ \phi_{24_i} + DLDP_i \\ DADV_i\ \dot{\phi}_{25_i} + DADR_i\ \phi_{25_i} + DGDP_i \end{bmatrix}^T \tag{5.2.22}
$$

After rearranging this equation, we get

$$
\dot{\phi}_{\overline{v}_i} = DADV_i\ \dot{\phi}_{\overline{v}_i} + DADR_i\ \phi_{\overline{r}_i} + \begin{bmatrix} 0_{3x3} & 0_{3x3} & DLDP_i & DGDP_i \end{bmatrix} \tag{5.2.23}
$$

Eq. (5.2.23) represents $3 \times (6 + n_{ldp_i} + n_{gdp_i})$ first order differential equations for the i-th satellite. Therefore, the total number of equations for ns satellites becomes $\sum_{i=1}^{ns} 3 \times (6 + n_{ldp_i} + n_{gdp_i})$.

Since multi-satellite orbit determination problem includes different types of satellites in terms of their perturbations and integration step size, a class of satellite is defined as a group of satellites which will use the same size of geopotential perturbation and the same integration order and step size. For l-classes of satellites, the integration vector, X_{INT}, is defined as

$$
X_{INT} \equiv
\begin{bmatrix}
\bar{r}_{11} \\
\vdots \\
\bar{r}_{1ns_1} \\
\hline
\phi_{\bar{r}_{11}} \\
\vdots \\
\phi_{\bar{r}_{1ns_1}} \\
\hline
\bar{v}_{11} \\
\vdots \\
\bar{v}_{1ns_1} \\
\hline
\phi_{\bar{v}_{11}} \\
\vdots \\
\phi_{\bar{v}_{1ns_1}} \\
\hline
\vdots \\
\hline
\bar{r}_{l1} \\
\vdots \\
\bar{r}_{lns_l} \\
\hline
\phi_{\bar{r}_{l1}} \\
\vdots \\
\phi_{\bar{r}_{lns_l}} \\
\hline
\bar{v}_{l1} \\
\vdots \\
\bar{v}_{lns_l} \\
\hline
\phi_{\bar{v}_{l1}} \\
\vdots \\
\phi_{\bar{v}_{lns_l}}
\end{bmatrix}
\tag{5.2.24}
$$

where ns_i is the number of satellites for i-th class, $\bar{r}_{ij}$ and $\bar{v}_{ij}$ are the position and velocity of the j-th satellite of i-th class, respectively. $\phi_{\bar{r}_{ij}}$ is the state transition matrix

for the j-th satellite's positions of i-th class and $\phi_{\overline{v}_{ij}}$ is the state transition matrix for the j-th satellite's velocities of i-th class.

$$
\dot{X}_{INT} = \begin{bmatrix}
\overline{v}_{11} \\
\vdots \\
\overline{v}_{1ns_1} \\
\hdashline
\phi_{\overline{v}_{11}} \\
\vdots \\
\phi_{\overline{v}_{1ns_1}} \\
\hdashline
\overline{f}_{11} \\
\vdots \\
\overline{f}_{1ns_1} \\
\hdashline
\dot{\phi}_{\overline{v}_{11}} \\
\vdots \\
\dot{\phi}_{\overline{v}_{1ns_1}} \\
\hdashline
\vdots \\
\hdashline
\overline{v}_{l1} \\
\vdots \\
\overline{v}_{lns_l} \\
\hdashline
\phi_{\overline{v}_{l1}} \\
\vdots \\
\phi_{\overline{v}_{lns_l}} \\
\hdashline
\overline{f}_{l1} \\
\vdots \\
\overline{f}_{lns_l} \\
\hdashline
\dot{\phi}_{\overline{v}_{l1}} \\
\vdots \\
\dot{\phi}_{\overline{v}_{lns_l}}
\end{bmatrix}
\qquad (5.2.25)
$$

Eq. (5.2.25) is numerically integrated using a procedure such as the Krogh-Shampine-Gordon fixed-step fixed-order formulation for second-order differential equations [*Lundberg*, 1981] for each class of satellites. For the ICESat/GLAS-GPS case, two classes of satellites need to be defined. One is for the high satellites, e.g. GPS, and the other is for the low satellite, e.g. ICESat/GLAS.

5.3   Output

Although a large number of parameters are available from the estimation process as given by Eq. (5.2.24), the primary data product required for the generation of other products is the ephemeris of the ICESat/GLAS spacecraft center of mass. This ephemeris will be generated at a specified interval, e.g., 30-sec and will include the following:

t in GPS time

3 position components of the spacecraft center of mass in ICRF and ITRF

T_{ICRF}^{ITRF} the 3×3 transformation matrix between ICRF and the ITRF.

The output quantities will be required at times other than those contained in the generated ephemeris file. Interpolation methods, such as those examined by *Engelkemier* [1992] provide the accuracy comparable to the numerical integration accuracy itself. With these parameters the ITRF position vector can be obtained as well by forming the product of the transformation matrix and the position vector in ICRF.

6.0   IMPLEMENTATION CONSIDERATIONS

In this chapter, some considerations for implementing ICESat/GLAS POD algorithms are discussed. Section 6.1 describes the POD software system in which the POD algorithms are implemented, and the necessary input files for the software are defined. Section 6.2 describes the POD products. Section 6.3 describes the ICESat/GLAS orbit and attitude. Section 6.4 discusses the expected ICESat/GLAS orbit accuracy based on simulations. Section 6.5 summarizes the POD processing strategies.   Section 6.6 discusses the plans for pre-launch and post-launch POD activities. Section 6.7 considers computational aspects.

6.1   POD Software System

The POD algorithms described in the previous chapters were implemented in a software system, referred to as MSODP1 (Multi-Satellite Orbit Determination Program 1). This software has been developed by the Center for Space Research (CSR), and shares heritage with UTOPIA [*Schutz and Tapley*, 1980a]. This software can process SLR data and Doppler data in addition to GPS pseudo-range and double-differenced carrier phase data. A version of this POD software will be placed under change control at ICESat/GLAS launch. MSODP1 requires input files, some of which define model parameters, and the following section discusses these necessary input files.

6.1.1   Ancillary Inputs

Some model parameters require continual updating through acquisition of input information hosted on various standard anonymous ftp sites. This includes the Earth orientation parameters, x_p, y_p, and UT1, and solar flux data. Other files, which are considered to be static once "tuned" to ICESat/GLAS requirements include the planetary ephemerides, geopotential parameters, and ocean tides parameters,. In addition, information about the spacecraft attitude is required for the box-wing spacecraft model in the computation of non-gravitational forces and to provide the correction for the GPS phase center location with respect to the spacecraft center of mass. The real-time attitude obtained during flight operations is thought to be adequate for this purpose, but it will be checked against the precise attitude during the Verification Phase. Also, the GPS data from the IGS ground network and the ICESat/GLAS receiver, and SLR data from the International Laser Ranging Service (ILRS) are needed.

6.2   POD Products

Two types of POD products will be generated: the Rapid Reference Orbit (RRO) and the operational POD. The former product will be generated within 12-24 hours for primarily internal use of assessing the operational orbit and verification support for mission planning. The operational POD will be generated within 14 days, possibly within 3 days, after accounting for problems identified in RRO (e.g. GPS satellite problems) and problems reported by IGS. This product will be used in

generating the altimetry standard data products, particularly level 1B and level 2 surface elevation products.

6.3   ICESat/GLAS Orbit and Attitude

During the first 30-150 days after launch, the ICESat/GLAS spacecraft will be operated in a calibration orbit, with an 8-day repeat ground-track interval and 94-degree inclination.   At some point during this period to be determined by calibration results, the orbit will be transitioned to a neighboring mission orbit at the same inclination, with a 183-day repeating ground track.   The ICESat/GLAS operational scenarios and orbit parameters are summarized in Table 6.1.

Table 6.1 ICESat/GLAS Orbit Parameters

Mission Phase	Expected Duration (days)	Mean Altitude (km)	Inclina- tion (deg)	Eccen- tricity	Ground Track Repeat Cycle
S/C Checkout	30	600	94	0.001	No requirement
Calibration/ Validation	31-150	600	94	0.0013	8 days/183 days
Polar Mapping	151-1220	600	94	0.0013	183 days with 25 and 8 day sub-cycles

The ICESat/GLAS spacecraft will operate in two attitude modes depending on the angular distance between the orbit plane and the Sun (β' angle). As shown in Figure 1, for low-β' periods, such as that immediately following launch, the so-called "airplane-mode" is in use, with the solar panels perpendicular to the orbit

plane. When the β′ angle exceeds 32 degrees, however a yaw maneuver places the satellite in the "sailboat-mode", with the axis of solar panels now in the orbit plane. While the two attitudes ensure that the solar arrays produce sufficient power year-round for bus and instrument operations, they introduce significantly different atmospheric drag effects due to the difference in cross-sectional area perpendicular to the velocity vector.

6.4   POD Accuracy Assessment

The predicted radial orbit errors based on recent gravity models (e.g., JGM-3 or EGM-96) are 19-36 cm. To reduce the effect of the geopotential model errors on ICESat/GLAS, which is the major source of orbit error for ICESat/GLAS POD, the gravity model improvement effort will be made through gravity tuning. Solar activity is predicted to peak shortly after launch, and decline significantly during the mission. The level of this activity correlates directly with the magnitude of atmospheric drag effects on the satellite. The combinations of high solar flux and low β′ angle at the start of the mission poses special challenges for POD and gravity tuning.

A previous simulation study [*Rim et al.,* 1996] indicated that the ICESat/GLAS POD requirements could be met at 700-km altitude by either the gravity tuning or employing frequent estimation of empirical parameters, such as adjusting one-cycle-per-revolution parameters for every orbital revolution, within the context of a fully dynamic approach. This approach is referred to as a highly parameterized dynamic approach. Because the mission orbit altitude was lowered to

600-km, and the satellite design has been changed since this earlier study, a new in-depth simulation study [*Rim et al*., 1999] was conducted. It also indicates that even at 600-km altitude with maximum solar activity, the 5-cm and 20-cm radial and horizontal ICESat/GLAS orbit determination requirement can be met using this aforementioned gravity tuning and fully dynamical reduction strategy. Table 6.2 summarizes the ICESat/GLAS orbit accuracy based on two geopotential models, pre-tune and post-tune models. The results are based on eight 1-day arcs with three different parameterizations. Those are (A) 1-rev C_d, 6-hour 1cpr TN, (B) 1-rev C_d, 3-hour 1cpr TN, and (C) 1-rev C_d, 1-rev 1cpr TN, where 1-rev C_d indicates solving for drag coefficient for every orbital revolution, and 1cpr TN means solving for one-cycle-per-revolution Transverse and Normal parameters. Note that even the case (C) could not meet the radial orbit determination requirement using the pre-tune geopotential model. This indicates that gravity tuning is necessary to achieve the orbit determination requirement. A factor of three improvement in radial orbit accuracy was achieved for case (A), and a factor of two improvement occurred for case (C) by the post-tune gravity field.

Table 6.2 ICESat/GLAS Orbit Errors (cm)

Case	Pre-Tune				Post-Tune			
	Data	RMS Orbit Errors			Data	RMS Orbit Errors		
	RMS	R	T	N	RMS	R	T	N
A	5.0	15.5	35.2	14.1	1.9	5.2	11.2	5.6
B	3.6	10.3	22.4	11.2	1.7	3.6	10.7	5.4
C	2.3	6.5	12.2	5.9	1.6	3.3	10.1	5.2

6.5   POD Processing Strategy

6.5.1   Assumptions and Issues

Several assumptions were made for the POD processing. We assume: 1) continued operation of IGS GPS network and the SLR network, 2) IGS GPS data is available in RINEX (Receiver Independent Exchange) format, 3) ICESat/GLAS GPS receiver has performance characteristics comparable to the flight TurboRogue, and ICESat/GLAS GPS data are available in RINEX format, and 4) most relevant IGS, SLR and ICESat/GLAS data are available within 24-36 hours. There are several issues for POD processing which include: 1) identification of problem GPS satellites, 2) identification of problems with ground station data, 3) processing arc length, 4) accommodation for orbit maneuvers, and 5) problems associated with expected out-gassing during early mission phase. For a July 2001 launch and the early phases of the mission, orbit maneuvers are expected to occur as frequently as 5 days because of high level of solar activity [*Demarest and Schutz*, 1999]. These maneuvers will not be modeled, but the maneuver times will be utilized to reinitialize the orbit arc length.

6.5.2   GPS Data Preprocessing

The GPS data processing procedure consists of two major steps: data preprocessing and data reduction. The data preprocessing step includes data acquisition, correcting measurement time tags, generating double-differenced observables, and data editing. The GPS data preprocessing system is collectively

called TEXGAP (university of TEXas Gps Analysis Program) and implemented on the HP workstation.

The International GPS Service for Geodynamics (IGS) provides GPS data collected from globally distributed GPS tracking sites, which include more than 200 ground stations at present [*IGS*, 1998]. The daily IGS data files are archived in the IGS global data centers in the RINEX format, and the data from selected ground station network will be downloaded to CSR's data archive system. Also, the GPS data from the ICESat/GLAS GPS receiver will be provided by the ICESat Science Investigator Processing System.

The GPS receiver time tag is in error due to the receiver clock error, and the time tag correction, t_r, can be obtained by

$$t_r = \rho/C - \rho_c/C + t_s \tag{6.1}$$

where C is the speed of light, ρ is the pseudorange measurement, ρ_c is the computed range from GPS ephemerides and receiver position, and t_s is the broadcast GPS satellite clock correction.

Double-differencing eliminates common errors, such as the GPS satellite and receiver clock errors, including the Selective Availability (SA) effect. As described in Section 4.2.3, a double-differenced high-low observation consists of a ground station, two GPS satellites, and ICESat/GLAS satellite. A careful selection of double-differenced combination is required to avoid generating dependent data set.

To eliminate the first-order ionospheric effects, the double-differenced carrier phase observables DD_{L1} at L_1 and DD_{L2} at L_2 frequency are combined to form the ionosphere-free observable, DD_{Lc}, as follows:

$$DD_{Lc} = \frac{f_{L1}^{2}}{f_{L1}^{2} - f_{L2}^{2}} DD_{L1} - \frac{f_{L1} f_{L2}}{f_{L1}^{2} - f_{L2}^{2}} DD_{L2} \tag{6.2}$$

where f_{L1} = 1575.42 MHz and f_{L2} = 1227.60 MHz.

Data editing involves the detection and fixing of the cycle-slips of the carrier phase data, and the editing of data outliers. For editing outliers, a 3σ editing criterion is applied to the double-differenced residual. Cycle-slips are detected by examining the differences between the consecutive data points in the double-differenced residuals and identifying discontinuity. The identified cycle-slips are fixed by using linear extrapolations.

6.5.3 GPS Orbit Determination

ICESat/GLAS POD requires precise GPS ephemerides, and there are two approaches to obtain the precise GPS ephemerides. The first approach is to solve the GPS orbit simultaneously with the ICESat/GLAS orbit, and the second approach is to fix the GPS ephemeris to an independent determination, such as the IGS solutions. For the first approach, standard models described in Table 6.3 will be used for the reference frame and gravitational perturbations for GPS. For the non-gravitational perturbations on GPS, the models described in Section 3.4.5 will be employed. It has been shown for the Topex POD case that adjusting GPS orbits usually resulted better Topex orbit solutions [*Rim et al*., 1995]. A simulation study [*Rim et al*., 2000b] indicates that fixing GPS orbits to high accuracy solutions would generate reasonably well-tuned gravity field, thereby, the POD accuracy requirement could be met with fixing GPS approach. As the accuracy of IGS solutions improved significantly [*Kouba et al*., 1998], fixing GPS ephemeris to IGS solutions would be a preferred approach for ICESat/GLAS POD. These two approaches will be evaluated using

available tracking data during the pre-launch period, such as CHAMP and JASON, and ICESat/GLAS tracking data during the verification/validation period.

6.5.4 Estimation Strategy

The adopted estimation strategy for ICESat/GLAS POD is the dynamic approach with tuning of model parameters, especially the geopotential parameters. Simulation studies indicate that frequent estimation of empirical parameters is an effective way of reducing orbit errors. The solutions from the sequential filter with process-noise will be investigated as a validation tool for the highly parameterized dynamic solutions. Results of *Davis* [1996] and *Rim et al.* [2000a] show that both highly parameterized dynamic approach with gravity tuning and the reduced-dynamic approach yield comparable results in high fidelity simulations. This comparison will continue with the flight data.

6.6   POD Plans

This section describes planned POD activities during the pre-launch and the post-launch periods.

6.6.1 Pre-Launch POD Activities

During the pre-launch period, POD activities will be focused on the following areas: 1) selection of POD standards, 2) model improvement efforts, 3) preparation for operational POD, and 4) POD accuracy assessment. In this section, pre-launch POD activities in these areas are summarized.

6.6.1.1   Standards

The standard models for the reference system, the force models and the measurement models to be used for the ICESat/GLAS POD are described in Table 6.3. These standards are based on the International Earth Rotation Service (IERS) Conventions [*McCarthy,* 1996], and the T/P standards [*Tapley et al.,* 1994]. These standards will be updated as the models improve, and "best" available models at launch will be selected as the initial standard models.

Table 6.3 Precision Orbit Determination Standards for ICESat/GLAS

Model	ICESat/GLAS Standard	Reference
Reference Frame		
Conventional inertial system	ICRF	IERS
Precession	1976 IAU	IERS
Nutation	1980 IAU	IERS
Planetary ephemerides	JPL DE-405	Standish [1998]
Polar Motion	IERS	
UT1-TAI	IERS	
Station Coordinates	ITRF	
Plate motion	Nuvel (NNR)	IERS
Reference ellipsoid	a_e = 6378136.3 m	Wakker [1990]
	1/f = 298.257	
Force Models		
GM	398600.4415 km^3/s^2	Ries et al. [1992a]
Geopotential	JGM-3	Tapley et al. [1996]
	or EGM-96	Lemoine et al. [1996]
$\overline{C}_{21}$, $\overline{S}_{21}$ – mean values	$\overline{C}_{21}$ = -0.187×10^{-9}	
	$\overline{S}_{21}$ = +1.195×10^{-9}	
$\dot{\overline{C}}_{21}$, $\dot{\overline{S}}_{21}$ – rates	$\dot{\overline{C}}_{21}$ = -1.3×10^{-11}/yr	(see rotational deformation)
	$\dot{\overline{S}}_{21}$ = +1.1×10^{-11}/yr	
	epoch 1986.0	
Zonal rates	$\dot{J}_2$ = -2.6×10^{-11}/yr	Nerem et al. [1993]
	epoch 1986.0	
N body	JPL DE-405	Standish [1998]
Indirect oblateness	point mass Moon on Earth J_2	
Solid Earth tides		IERS–Wahr [1981]
Frequency independent	k_2 = 0.3, k_3 = 0.093	
Frequency dependent	Wahr's theory	
Ocean tides	CSR TOPEX_3.0	Eanes and Bettadpur [1995]
Rotational deformation	$\Delta\overline{C}_{21}$ = -1.3×10^{-9}$(x_p - \overline{x}_p)$	Nerem et al. [1994]
	$\Delta\overline{S}_{21}$ = +1.3×10^{-9}$(y_p - \overline{y}_p)$	
	based on k_2/k_0 = 0.319	
	$\overline{x}_p$ = 0".046, $\overline{y}_p$ = 0".294	
	$\dot{\overline{x}}_p$ = 0".0033/yr	
	$\dot{\overline{y}}_p$ = 0".0026/yr, epoch 1986.0	
Relativity	all geocentric effects	Ries et al. [1991]
Solar radiation	solar constant = 4.560×10^{-6}	
	N/m^2 at 1 AU, conical shadow	
	model for Earth and Moon	
	R_e = 6402 km,	
	R_m = 1738 km,	

	R_s = 696,000 km	
Atmospheric drag	density temperature model	Barlier et al. [1977]
	or MSIS90	Hedin [1991]
	daily flux and 3-hour	
	constant k_p,	
	3-hour lag for k_p;	
	1-day lag for $f_{10.7}$,	
	$\bar{f}_{10.7}$ average of previous 81 days	
Earth radiation pressure	Albedo and infrared second-degree	Knocke et al. [1989]
	zonal model, R_e = 6378136.3 m	
Satellite parameters	ICESat/GLAS models	
	Box-wing model	

Measurement Models

Laser range		
Troposphere	Marini & Murray [1973]	IERS
Relativity correction	applied	IERS
Center of Mass/phase center	ICESat/GLAS model	
GPS		
Troposphere	MTT	Herring [1992]
Ionosphere	dual frequency correction	
Center of Mass/phase center	ICESat/GLAS model	
Relativity correction	applied	
Site displacement		
Induced permanent tide	IERS	
Geometric tides		
Frequency independent	$h_2 = 0.6090$,	IERS
	$l_2 = 0.0852$,	
	$\delta = 0°$	
Frequency dependent	K_1 only	IERS
Ocean loading	IERS	
Rotational deformation	$h_2 = 0.6090$, $l_2 = 0.0852$ with	IERS
	$\bar{x}_p = 0".046$, $\bar{y}_p = 0".294$	
	$\dot{\bar{x}}_p = 0".0033/\text{yr}$	
	$\dot{\bar{y}}_p = 0".0026/\text{yr}$, epoch 1986.0	

Figures 2 and 3 show the ground station network for ICESat/GLAS POD for GPS and SLR, respectively. Details of the adopted network may change prior to launch but will remain quite robust. Station coordinates will be adopted from the "best" available ITRF model, expected to be ITRF-99 or ITRF-2000. The ITRF model includes station velocities measured by space geodetic methods.

6.6.1.2   *Gravity Model Improvements*

The gravity model to be used in the immediate post-launch period will be "best" available at launch, such as JGM-3 [*Tapley et al*., 1996] or EGM-96 [*Lemoine et al*., 1996]. As further gravity model improvements are made from other projects, such as GRACE, they will be incorporated for ICESat/GLAS POD. At this writing, further study is required for the selection of the at-launch gravity model. However, current state-of-the-art models are sufficiently close that geopotential tuning with ICESat/GLAS data should yield comparable POD performance which is largely unaffected by this initial selection. The "best" available ocean tide model at launch will be adopted as the standard ocean tide model for ICESat/GLAS POD.

6.6.1.3   *Non-Gravitational Model Improvements*

Since the ICESat/GLAS launch coincides with the predicted solar maximum, the atmospheric drag perturbation will be the largest non-gravitational force acting on the satellite. Some drag-related models will be evaluated as part of drag model improvement efforts for reducing the effect of drag model errors on POD. Those include the thermospheric wind model, HWM93 [*Hedin et al*., 1996] and free

molecular flow drag model [*Fredo*, 1980]. Estimation strategies to minimize the effects of drag model errors on POD and gravity tuning will also be investigated.

In order of decreasing magnitude, the remaining non-gravitational perturbations consist of solar radiation pressure, Earth radiation pressure, and on-board thermal emission. For POD, a 'box-wing' model, described in Section 3.4.6, represents the spacecraft as a simple combination of a six-sided box and two attached panels, or 'wings'. This macro-model will use effective specular and diffuse reflectivity coefficients to compute the induced forces acting on each surface. The pre-flight values of these coefficients will be estimated during a tuning process, in which the forces computed with the macro-model are fit to those obtained using a separate micro-model [*Webb*, private communication, 2000]. This latter model employs considerable detail that makes it impractical for use directly in POD. Once ICESat/GLAS is in orbit, the reflectivity coefficients will be adjusted during POD, using the GPS tracking data.

The macro-model tuning effort will compute the radiation from various sources incident on the satellite's surfaces. By using a comprehensive thermal model, the propagation of this energy throughout the spacecraft will be calculated. The resulting temperature distribution will be evaluated to determine whether any on-board thermal gradients may induce net forces. Any such forces would then be modeled analytically during POD.

The non-gravitational forces acting on each surface due to atmospheric drag, solar radiation pressure, Earth radiation pressure, and thermal emission are computed individually and then summed to obtain the total non-gravitational force acting on the satellite.

6.6.1.4   Measurement Model Developments

One of the sources of measurement model errors is the multipath effect. Colorado Center for Astrodynamics Research (CCAR) multipath study [*Axelrad et al.*, 1999] indicates that the multipath effect alone results in 1-2 cm radial orbit error, while this effect in the presence of other errors, such as drag and gravitational model errors, results in a few mm error. This study was based on a preliminary design location for the antennas and most of the multipath effect was caused by the solar arrays. It also indicates that the effect becomes even smaller with proper editing scheme, such as blocking certain regions. The capability of screening out GPS measurements from blocked regions will be implemented in MSODP1. The final spacecraft design has the GPS antennas positioned above the solar array and bus star cameras. In this location, there is no expected impingement above the ground plane so multipath will be mitigated.

ICESat/GLAS satellite's center of mass location with respect to a reference point on the spacecraft will be measured in the pre-launch period, and the location of the GPS antenna and the laser reflector will also be measured. GPS antenna phase center variations as a function of azimuth and elevation will be determined in pre-launch testing. Expenditure of fuel and corresponding changes in center of mass location will be monitored during flight.

6.6.1.5   Preparation for Operational POD

To generate the POD products operationally when large volumes of data are required, it is essential to make the POD processing as automatic as possible. The POD processing procedures will be examined end-to-end to identify/update the

procedures for possible improvement and to minimize the human intervention, and computational and human resources will be allocated optimally for POD processing. The adopted operational POD processing procedures/scripts will be tested by processing upcoming satellites, such as JASON and CHAMP, during the pre-launch period for further improvement.

6.6.1.6   Software Comparison

Since the POD products from different software will be compared for POD validation, it is important to compare different software packages in the pre-launch period to identify model differences and to quantify the level of agreement among different POD software systems, such as UT-CSR's MSODP1, GSFC's GEODYN, and JPL's GOA II.   This comparison becomes easier for the ICESat/GLAS POD due to the extensive POD software comparison activity between UT-CSR and GSFC for Topex POD [*Ries*, 1992b].   Also, Topex-GPS POD experiments between UT-CSR and JPL [*Bertiger et al*., 1994] gave the opportunity for both groups to compare their software systems. This comparison will continue for the ICESat/GLAS POD models to ensure the validity of the POD verification by comparing with POD products from different software systems.

6.6.1.7   POD Accuracy Assessment

During the pre-launch period, simulation studies will continue to assess the POD accuracy. Comparison of highly parameterized dynamic approach and the reduced-dynamic approach will be continued. For the GPS orbit modeling, standard models for GPS orbit determination will be updated as the models progress, and the resulting orbit will be compared to the IGS solutions. Also, the effect of fixing GPS

orbits to independently determined ephemerides, such as IGS solutions, on the POD and the gravity tuning will be evaluated.

6.6.2 Post-Launch POD Activities

During the first 30-150 days after launch, which is the Calibration/Validation period, POD processing will tune the model parameters, including the gravity, and define adopted parameter set for processing the first 183-day cycle. During the 183 days of the Cycle 1, the POD processing will assess and possibly further improve or refine parameters, such as assess the gravity field from the gravity mission GRACE, if available, and adopt a new parameter set for the processing of Cycle 2 data. POD processing will continue assessment of POD quality after Cycle 1, and new parameter adoptions should be minimized and timed to occur at cycle boundaries.

6.6.2.1 Verification/Validation Period

During the calibration/validation period, several important POD activities will be undertaken simultaneously. These include tuning model parameters, POD calibration/validation, evaluation of out-gassing effect, evaluation of estimation strategies and GPS orbit modeling procedure, evaluation of multipath effect and construction of editing scheme.

Some model parameters, such as geopotential parameters and the "box-wing" model parameters, will be tuned using the tracking data. About 30-40 days of GPS data will be processed for gravity tuning, and the arc length will be dictated by the maneuver spacing and the ability of POD to mitigate the effect of the non-gravitational model errors, especially the drag model errors, to certain level. The

tuned gravity field will be determined by combining the pre-tune gravity coefficients and the solution covariance with the new information equations from the GPS tracking data.

Internal and external POD calibration/validation activities are planned for POD quality assessment, and those are summarized in the following section.

During the early phase of the mission, the satellite might experience significant out-gassing, and this poses serious challenges for POD. However, this effect will subside as time goes by, and every effort will be made to insure that this effect does not corrupt the parameter tuning process during this validation/verification period.

Estimation strategies described in Section 6.5.4 will be evaluated, and the GPS orbit modeling procedures described in Section 6.5.3 will also be evaluated during this period.

The multipath effect will be evaluated to characterize the extent of signal corruption due to diffraction and reflection using the flight data. Proper editing scheme will be developed if there is any evidence that such an editing reduces the multipath effect on POD.

6.6.2.2   POD Product Validation

To validate the accuracy of ICESat/GLAS POD products, several methods would be employed. For the internal evaluation of the orbit consistency, orbit overlap statistics will be analyzed. Also, the data fit RMS value is an effective indicator of orbit quality. Comparisons between the orbits from different software, such as MSODP1, GEODYN, and GIPSY-OASIS II (GOA II), would serve as a valuable tool

to assess the orbit accuracy. Since the ICESat/GLAS will carry the laser reflector on board, the SLR data can be used as an independent data set to determine the ICESat/GLAS orbit. However, this approach assumes reasonably good tracking of the ICESat/GLAS orbit from the SLR stations. Data from the SLR network will also be used to directly evaluate the GPS-determined orbit. Data fits for high elevation SLR passes can be used to evaluate the orbit accuracy of the ICESat/GLAS. The laser altimeter data will be used to assess the validation, however, this assessment can be accomplished only if the calibration and verification of the instrument have been accomplished. Global crossovers from ICESat/GLAS will be used to validate the radial orbit accuracy in a relative sense.

6.6.2.3   POD Reprocessing

To produce improved orbits, reprocessing of data will be performed as often as annually. As the solar activity is expected to decrease in the later mission period, the accuracy of the tuned model parameters will be improved, thereby the POD accuracy will be improved. Any improvement in the model parameters will be adopted for the reprocessing.

### 6.7   Computational: CPU, Memory and Disk Storage

Table 6.4 compares the computational requirements for processing a typical one-day arc from a 24-ground station network with 30 sec sampling time for both T/P and ICESat/GLAS. These results are based on MSODP1 implemented on the Cray J90 and the HP-735/125.

Current computational plans are to use the HP-class workstation environment for preprocessing GPS data, including generation of double difference files. POD processing will be performed on a Cray J90, or equivalent. This processing on the Cray enables a more efficient resource sharing with other project, such as GRACE.
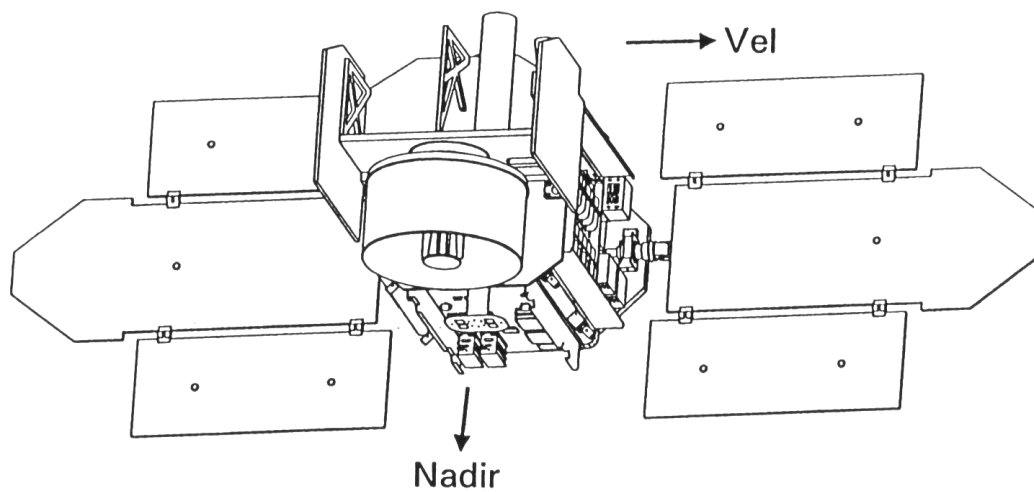
Table 6.4 Computational Requirements for T/P and ICESat/GLAS POD using MSODP1: One-day Arcs with 24 Ground Stations

Platform	Satellite	CPU (min)	Memory (Mw)	Disk* (Mb)
Cray J90	T/P	20	2	35
	ICESat/GLAS	40	2.5	59
HP-735	T/P	30	2	39
	ICESat/GLAS	105	2.5	63

* This includes all the necessary files.
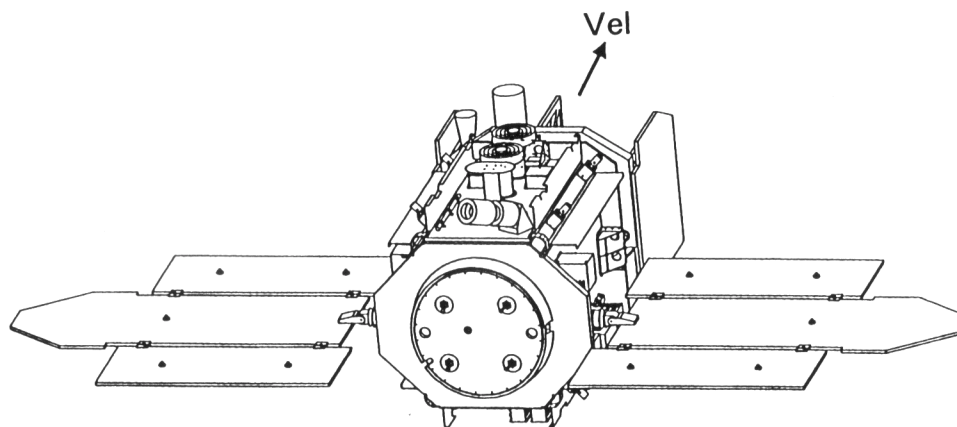
a) "airplane mode" for low β'

b) "sailboat mode" for high β'

Figure 1. ICESat/GLAS Operational Attitudes
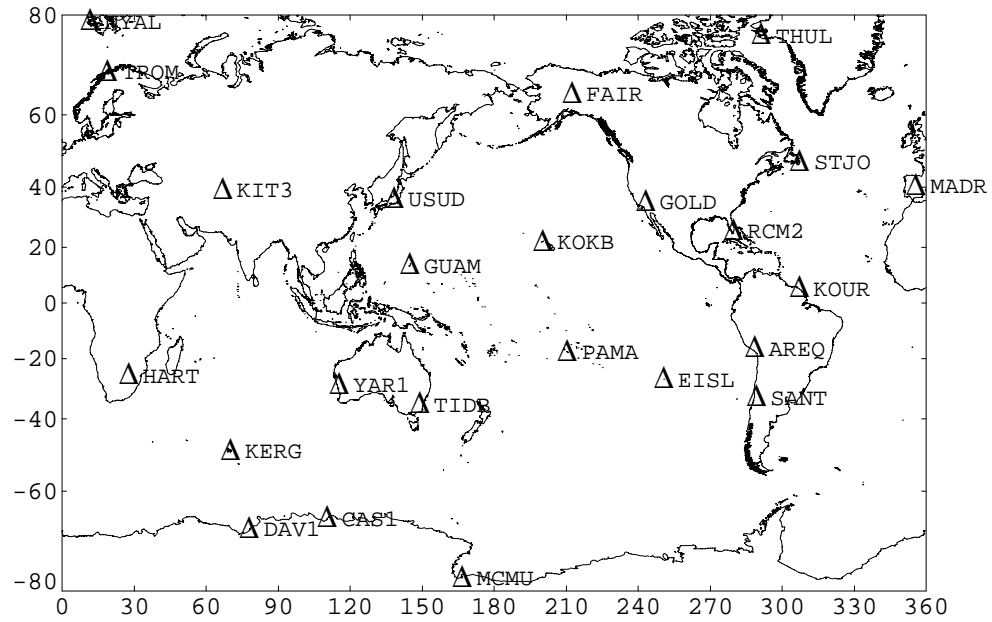
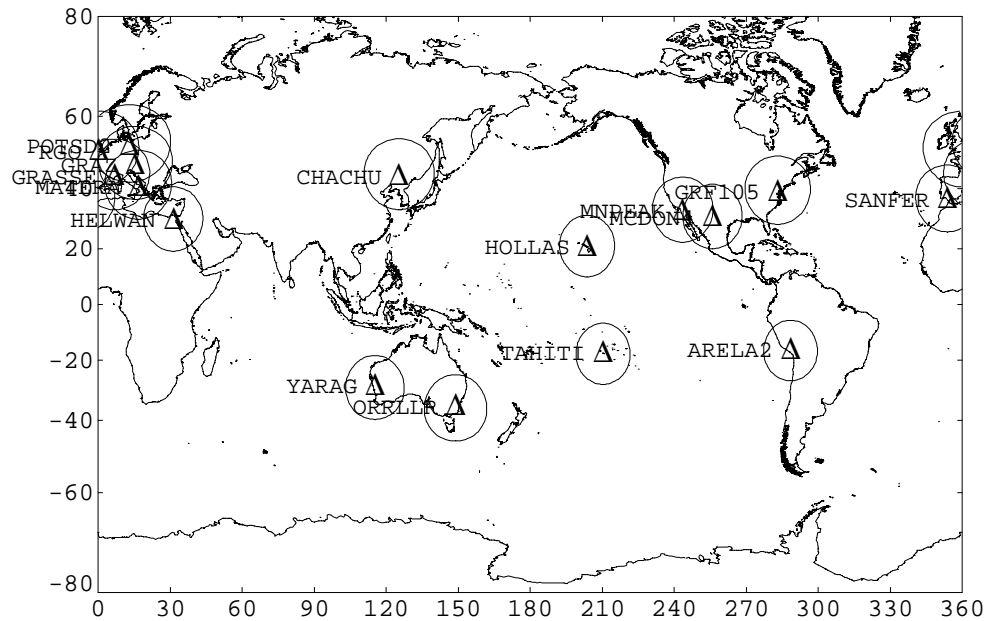**Figure 2. GPS Tracking Stations for ICESat/GLAS POD**

Figure 3. SLR Stations Tracking ICESat/GLAS (20 degree Elevation Masks)

7.0   BIBLIOGRAPHY

Anderle, R. J., Geodetic Analysis Through Numerical Integration, *Proceedings of the International Symposium on the Use of Artificial Satellites for Geodesy and Geodynamics*, Athens, Greece, 1973.

Antreasian, P. G. and G. W. Rosborough, Prediction of Radiant Energy Forces on the TOPEX/POSEIDON Spacecraft, *J. Spacecraft and Rockets*, Vol. 29, No. 1, 81-90, 1992.

Atlshuler, E. E., and P. M. Kalaghan, Tropospheric range error corrections for the NAVSTAR system, Air Force Cambridge Research Laboratories, *AFCRL-TR-74-0198*, April 1974.

Axelrad, P., K. Gold, P. Madhani, ICESat Observatory Multipath Effect, Final Report, Colorado Center for Astrodynamics Research, University of Colorado, March, 1999.

Barlier, F., C. Berger, J. L. Falin, G. Kockarts, and G. Thuiller, A Thermospheric Model Based on Satellite Drag Data, *Aeronomica Acta*, Vol. 185, 1977.

Bertiger, W. I., Y. E. Bar-Sever, E. J. Christensen, E. S. Davis, J. R. Guinn, B. J. Haines, R. W. Ibanez-Meier, J. R. Jee, S. M. Lichten, W. G. Melbourne, R. J. Mullerschoen, T. N. Munson, Y. Vigue, S. C. Wu, T. P. Yunck, B. E. Schutz, P. A. M. Abusali, H. J. Rim, M. M. Watkins, and P. Willis, GPS Precise Tracking of TOPEX/POSEIDON: Results and Implications, *J. Geophys. Res.*, 99, C12, 24449-24464, 1994.

Beutler, G., E. Brockmann, U. Gurtner, L. Hugentobler, L. Mervart, M. Rothacher, and A. Verdun, Extended Orbit Modeling Techniques at the CODE Processing Center of the International GPS Service for Geodynamics (IGS): Theory and the Initial Results, *Manuscripta Geodaetica, 19*, 367-386, 1994.

Byun, S. H., Satellite Orbit Determination Using GPS Carrier Phase in Pure Kinematic Mode, Dissertation, Department of Aerospace Engineering and Engineering Mechanics, The University of Texas at Austin, December, 1998.

Cartwright D. E. and R. J. Tayler, New Computations of the Tide Generating Potential, *Geophys. J. Roy. Astron. Soc.,* Vol. 23, 45-74, 1971.

Cartwright D. E. and A. C. Edden, Corrected Tables of Tidal Harmonics, *Geophys. J. Roy. Astron. Soc.,* Vol. 33, 253-264, 1973.

Cassoto, S., Ocean Tide Models for Topex Precise Orbit Determination, Dissertation, Department of Aerospace Engineering and Engineering Mechanics, The University of Texas at Austin, December 1989.

Chao, C. C., The Tropospheric Calibration Model for Mariner Mars 1971, *Technical Report 32-1587*, 61-76, JPL, Pasadena, California, March, 1974.

Christensen, E. J., B. J. Haines, K. C. McColl, and R. S. Nerem, Observations of Geographically Correlated Orbit Errors for TOPEX/Poseidon Using the Global Positioning System, *Geophys. Res. Let.*, *21(19)*, 2175-2178, Sep. 15, 1994.

Ciufolini, I., Measurement of the Lense-Thirring Drag on High-Altitude Laser-Ranged Artificial Satellites, *Phys. Rev. Let.*, *56*, 278, 1986.

Clynch J. R. and D. S. Coco, Error Characteristics of High Quality Geodetic GPS Measurements: Clocks, Orbits, and Propagation Effects, in *Proceedings of the 4th International Geodetic Symposium on Satellite Positioning*, Austin, Texas, 1986.

Colombo, O. L., Ephemeris Errors of GPS Satellites, *Bull. Geod., 60*, 64-84, 1986.

Colombo, O. L., The Dynamics of Global Positioning System Orbits and the Determination of Precise Ephemerides, *J. Geophys. Res.*, 94, B7, 9167-9182, 1989.

Davis, G. W., GPS-Based Precision Orbit Determination for Low Altitude Geodetic Satellites, *CSR-96-1*, May 1996.

Demarest, P. and B. E. Schutz, Maintenance of the ICESat Exact Repeat Ground Track, *Proc. AAS/AIAA Astrodynamics Specialist Conference*, Paper AAS 99-391, Girdwood, Alaska, August 16-19, 1999.

DeMets, C., R. G. Gordon, D. F. Argus, and S. Stein, Current Plate Motions, *Geophys J. R. Astron. Soc.*, 1990.

Dow, J. M., Ocean Tide and Tectonic Plate Motions from Lageos, Dissertation, Beim Fachbereich 12 - Vermessungswesen, der Technishen Hochshule Darmstadt, München, 1988.

Eanes, R. J., B. E. Schutz, and B. D. Tapley, Earth and Ocean Tide Effects on Lageos and Starlette, *Proceedings of the Ninth International Symposium on Earth Tides* (Ed. J. T. Kuo), 239-249, 1983.

Eanes, R. J. and S. Bettadpur, The CSR 3.0 Global Ocean Tide Model Diurnal and Semi-diurnal Ocean Tides from TOPEX/Poseidon Altimetry, *CSR-TM-96-06*, 1995.

Engelkemier, B. S., Lagrangian Interpolation to an Ordered Table to Generate a Precise Ephemeris, Thesis, The University of Texas at Austin, 1992.

Elyasberg, P., B. Kugaenko, V. Synitsyn, and M. Voiskovsky, Upper Atmosphere Density Determination from the COSMOS Satellite Deceleration Results, *Space Research*, Vol. XII, 1972.

Feulner, M. R., The Numerical Integration of Near Earth Satellite Orbits Across SRP Boundaries Using the Method of Modified Back Differences, Thesis, Department of Aerospace Engineering and Engineering Mechanics, The University of Texas at Austin, August 1990.

Finn, A. and J. Matthewman, A Single-Frequency Ionospheric Refraction Correction Algorithm for TRANSIT and GPS, in *Proceedings of the 5th International Geodetic Symposium on Satellite Positioning*, Las Cruces, New Mexico, March 13-17, 1989.

Fliegel H. F., T. E. Gallini, and E. R. Swift, Global Positioning System Radiation Force Model for Geodetic Applications, *J. Geophys. Res.*, *97,* 559-568, 1992.

Fredo, R. M., A Numerical Procedure for Calculating the Aerodynamic Coefficients for Complex Spacecraft Configurations in Free-Molecular Flow, Master's Thesis, Department of Aerospace Engineering, Pennsylvania State University, August, 1980.

Gibson, L. R., A Derivation of Relativistic Effect in Satellite Tracking, *Technical Report 83-55*, NSWC, Dahlgren, Virginia, April, 1983.

Goad, C. C. and L. Goodman, A Modified Hopfield Tropospheric Refraction Correction Model, presented at the AGU Fall Meeting, San Francisco, Calif., December 1974.

Goad, C. C., Gravimetric Tidal Loading Computed from Integrated Green's Functions, *J. Geophys. Res.*, *85*, 2679-2683, 1980.

Hedin, A. E., Extension of the MSIS Thermosphere and Exosphere with Empirical Temperature Profiles, *J. Geophys. Res.*, 96, 1159-1172, 1991.

Hedin, A. E., E. L. Fleming, A. H. Manson, F. J. Schmidlin, S. K. Avery, R. R. Clark, S. J. Franke, G. J. Fraser, T. Tsuda, F. Vidal, and R. A. Vincent, Empirical Wind Model for the Upper, Middle and Lower Atmosphere, *J. Atmos. Terr. Phys.*, 58, 1421-1447, 1996.

Heiskanen, W. A. and H. Moritz, *Physical Geodesy*, W. H Freeman and Company, London, 1967.

Herring, T. A., B. A. Buffett, P. M. Mathews, and I. I. Shapiro, Forced Nutations of the Earth: Influence of Inner Core Dynamics 3. Very Long Interferometry Data Analysis, *J. Geophys. Res.*, *96*, 8259-8273, 1991.

Herring, T. A., Modeling Atmospheric Delays in the Analysis of Space Geodetic Data, in *Refraction of Transatmospheric Signals in Geodesy*, J. De Munck and T. Spoelstra (ed.), Netherland Geodetic Commission Publications in Geodesy, 36, 157-164, 1992.

Hofmann-Wellenhof, B., H. Lichtenegger, and J. Collins, *GPS Theory and Practice*, Springer-Verlag Wien, New York, 1992.

Holdridge, D. B., An Alternate Expression for Light Time Using General Relativity, *JPL Space Program Summary 37-48*, III, 2-4, 1967.

Huang, C. and J. C. Ries, The Effect of Geodesic Precession in the Non-Inertial Geocentric Frame, *CSR-TM-87-04*, Center for Space Research, The University of Texas at Austin, December, 1987.

Huang, C., J. C. Ries, B. D. Tapley, and M. M. Watkins, Relativistic Effects for Near-Earth Satellite Orbit Determination, *Celestial Mechanics*, Vol. 48, No. 2, 167-185, 1990.

IGS, International GPS Service for Geodynamics: Resource information, 1998.

Jacchia, L. G., Revised Static Models of the Thermosphere and Exosphere with Empirical Temperature Profiles, *Smith. Astrophys. Obs. Spec. Rep.*, 332, 1971.

Jacchia, L. G., Thermospheric Temperature Density, and Composition: New Models, *Smith. Astrophys. Obs. Spec. Rep.*, 375, 1977.

Kaula, W. M., *Theory of Satellite Geodesy*, Blaisdell, Waltham, Mass., 1966.

Knocke, P. C. and J. C. Ries, Earth Radiation Pressure Effects on Satellites, University of Texas Center for Space Research Technical Memorandum, *CSR-TM-87-01*, September, 1987.

Knocke, P. C., Earth Radiation Pressure Effects on Satellite, Dissertation, Department of Aerospace Engineering and Engineering Mechanics, The University of Texas at Austin, May, 1989.

Kouba, J., Y. Mireault, G. Beutler, T. Springer, and G. Gendt, A Discussion of IGS Solutions and Their Impact on Geodetic and Geophysical Applications, *GPS Solutions*, Vol. 2, No. 2, 3-15, Fall 1998.

Lambeck, K., *The Earth's Variable Rotation: Geophysical Causes and Consequences*, Cambridge University Press, 1980.

Lawson, C. L. and R. J. Hanson, *Solving Least Squares Problems*, Prentice-Hall Inc., Englewood Cliffs, New York, 1974.

Lemoine, F. G., E. C. Pavlis, S. M. Klosko, N. K. Pavlis, J. C. Chan, S. Kenyon, R. Trimmer, R. Salman, R. H. Rapp, and R. S. Nerem, Latest Results from the Joint NASA GSFC and DMA Gravity Model Project, *EOS Transactions, AGU*, *77(17)*, p. S41, 1996.

Lieske, J. H., T. Lederle, W. Fricke, and B. Morando, Expressions for the precession quantities based upon the IAU (1976) System of Astronomical Constants, *Astronomy and Astrophysics*, Vol. 58, 1-16, 1977.

Lieske, J. H. Precession matrix based on IAU (1976) system of astronomical constants, *Astronomy and Astrophysics*, Vol. 73, 282-284, 1979.

Lundberg, J. B., Numerical Integration Techniques for Satellite Orbits, Univ. of Texas at Austin, Department of Aerospace Engineering and Engineering Mechanics, *IASOM-TR-81-1*, 1981.

Lundberg, J. B., Computational Errors and their Control in the Determination of Satellite Orbits, Report *CSR-85-3*, The Center for Space Research, The University of Texas at Austin, 1985.

Marini, J. W. and C. W. Murray, Correction of Laser Range Tracking Data for Atmospheric Refraction at Elevations above 10 Degrees, *Rep. X-591-73-351*, Goddard Space Flight Center, Greenbelt, Maryland, November 1973.

Marshall, J. A., S. B. Luthcke, P. G. Antreasian, and G. W. Rosborough, Modeling Radiation Forces Acting on TOPEX/Poseidon for Precise Orbit Determination, *NASA Technical Memorandom 104564*, June 1992.

McCarthy J. J. and T. V. Martin, A Computer Efficient Model of Earth Albedo Satellite Effects, NASA Goddard Space Flight Center, Planetary Sciences Department Report No. 012-77, June, 1977.

McCarthy D. D. (Ed.), IERS Conventions (1996), *IERS Tech. Note 21*, Obs. de Paris, July 1996.

Melbourne, W. G., E. S. Davis, T. P. Yunck, and B. D. Tapley, The GPS Flight Experiment on TOPEX/Poseidon, *Geophys. Res. Let.*, Vol. 21, No. 19, 2171-2174, Sep. 15, 1994.

Milani, A., Non-Gravitational Perturbations and Satellite Geodesy, Adam Hilger, 1987.

Milliken, R. J. and C. J. Zoller, Principle of Operation of NAVSTAR and System Characteristics, *Navigation*, Vol. 25, 95-106, 1978.

Minster, J. B., and T. H. Jordan, Present Day Plate Motions, *J. Geophys. Res.*, *83*, 5331-5354, 1978.

Moyer, T. D., Transformation from Proper Time on Earth to Coordinate Time in Solar System Barycentric Space-Time Frame of Reference. Part 1 & Part 2, *Celestial Mechanics*, Vol. 23, 33-56, 57-68, 1981.

Nerem, R. S., B. F. Chao, A. Y. Au, J. C. Chan, S. M. Klosko, N. K. Pavlis, and R. G. Williamson, Time Variations of the Earth's Gravitational Field from Satellite Laser Ranging to LAGEOS, *Geophys. Res. Lett., 20(7)*, 595-598, 1993.

Nerem, R. S., F. J. Lerch, J. A. Marshall, E. C. Pavlis, B. H. Putney, B. D. Tapley, R. J. Eanes, J. C. Ries, B. E. Schutz, C. K. Shum, M. M. Watkins, S. M. Klosko, J. C. Chan, S. B. Luthcke, G. B. Patel, N. K. Pavlis, R. G. Williamson, R. H. Rapp, R. Biancale, and F. Nouel, Gravity Model Development for TOPEX/POSEIDON: Joint Gravity Models 1 and 2, *J. of Geophys. Res., 99*, 24421-24447, 1994.

Remondi, B. W., Using the Global Positioning System (GPS) Phase Observable for Relative Geodesy: Modeling, Processing, and Results, Dissertation, Department of Aerospace Engineering and Engineering Mechanics, The University of Texas at Austin, May, 1984.

Ries, J. C., C. Huang, and M. M. Watkins, Effect of General Relativity on a near-Earth satellite in the geocentric and barycentric reference frames, *Phys. Rev. Lett., 61*, 903, 1988.

Ries, J. C., Simulation of an Experiment to Measure the Lense-Thirring Precession Using a Second Lageos Satellite, Dissertation, Department of Aerospace Engineering and Engineering Mechanics, The University of Texas at Austin, December, 1989.

Ries, J. C., C. Huang, M. M. Watkins, and B. D. Tapley, Orbit Determination in the Relativistic Geocentric Reference Frame, *J. Astron. Sci.*, *39(2)*, 173-181, 1991.

Ries, J. C., R. J. Eanes, C. K. Shum, and M. M. Watkins, Progress in the Determination of the Gravitational Coefficients of the Earth, *Geophys. Res. Lett., 19(6)*, 529-531, 1992a.

Ries, J. C. and D. Pavlis, TOPEX/POSEIDON Project, Software Intercomparison Results - Phase I and II, The University of Texas Center for Space Research, March 1992b.

Rim, H. J., B. E. Schutz, P. A. M. Abusali, and B. D. Tapley, Effect of GPS Orbit Accuracy on GPS-determined TOPEX/Poseidon Orbit, *Proc. ION GPS-95*, 613-617, Palm Springs, California, Sep. 12-15, 1995.

Rim, H. J., G. W. Davis, and B. E. Schutz, Dynamic Orbit Determination for the EOS Laser Altimeter Satellite (EOS ALT/GLAS) Using GPS Measurements, *J. Astron. Sci., 44(3)*, 409-424, 1996.

Rim, H. J., C. Webb, and B. E. Schutz, Analysis of GPS and Satellite Laser Ranging (SLR) Data for ICESat Precision Orbit Determination, *Proc. AAS/AIAA Space Flight Mechanics Meeting*, Paper 99-146, Breckenridge, Colorado, February 7-10, 1999.

Rim, H. J., C. Webb, S. Byun, and B. E. Schutz, Comparison of GPS-Based Precision Orbit Determination Approaches for ICESat, *Proc. AAS/AIAA Space Flight Mechanics Meeting*, Paper AAS-00-114, Clearwater, Florida, Jan. 24-26, 2000a.

Rim, H. J., C. Webb, and B. E. Schutz, Effect of GPS Orbit Errors on ICESat Precision Orbit Determination, *Proc. AIAA/AAS Astrodynamics Specialist Conference*, Paper AIAA-2000-4234, Denver, Colorado, Aug. 14-17, 2000b.

Schutz, B. E., and B. D. Tapley, Utopia: University of Texas Orbit Processor, Department of Aerospace Engineering and Engineering Mechanics, The University of Texas at Austin, *TR 80-1*, 1980a.

Schutz, B. E., and B. D. Tapley, Orbit Accuracy Assessment for Seasat, *J. Astron. Sci.,* Vol. XXVIII, No. 4, 371-390, October-December, 1980b.

Schutz, B. E., B. D. Tapley, R. J. Eanes, and M. M. Watkins, Earth Rotation from Lageos Laser Ranging, *Bureau International De L'Heure (BIH) Annual Report,* D51-D56, July, 1988.

Schutz, B. E., B. D. Tapley, P. A. M. Abusali, and H. J. Rim, Dynamic Orbit Determination Using GPS Measurements from TOPEX/Poseidon, *Geophys. Res. Let*., *21(19)*, 2179-2182, Sep. 15, 1994.

Seidelmann, P. K., 1980 IAU Theory of Nutation: The Final Report of the IAU Working Group on Nutation, *Celestial Mechanics*, Vol. 27, 79-106, 1982.

Shum, C. K., J. C. Ries, B. D. Tapley, P. Escudier, and E. Delaye, Atmospheric Drag Model for Precise Orbit Determination, *CSR-86-2*, Center for Space Research, The University of Texas of Austin, 1986.

Spilker, J. J., Jr., GPS Signal Structure and Performance Characteristics, *Navigation*, Vol. 25, 121-146, 1978.

Springer, T. A., G. Beutler and M. Rothacher, A New Solar Radiation Pressure Model for the GPS Satellites, IGS Workshop Proceedings, Darmstadt, Germany, ESOC, 1998.

Standish, E. M., JPL Planetary and Lunar Ephemerides DE405/LE405, *JPL Interoffice Memorandum, IOM 312.F-98-048*, Aug. 26, 1998 (Ephemerides available on CD-ROM).

Stephens G. L., G. G. Campbell, and T. H. Vonder Haar, Earth Radiation Budgets, *J. Geophys. Res.*, *86, C10*, 9739-9760, October, 1981.

Tapley, B. D., Statistical Orbit Determination Theory, *Advances in Dynamical Astronomy*, 396-425, B. D. Tapley and V. Szebehely, Eds., D. Reidel Publ. Co. Holland, 1973.

Tapley, B. D., B. E. Schutz, and R. J. Eanes, Station Coordinates, Baselines and Earth Rotation From Lageos Laser Ranging: 1976-1984, *J. Geophys. Res.*, *90*, 9235-9248, 1985.

Tapley, B. D. and J. C. Ries, Orbit Determination Requirements for TOPEX, *Proc. AAS/AIAA Astrodynamics Specialist Conference*, Paper 87-429, Kalispell, Montana, August 10-13, 1987.

Tapley, B. D., J. C. Ries, G. W. Davis, R. J. Eanes, B. E. Schutz, C. K. Shum, M. M. Watkins, J. A. Marshall, R. S. Nerem, B. H. Putney, S. M. Klosko, S. B. Luthcke, D. Pavlis, R. G. Williamson, and N. P. Zelensky, Precision Orbit Determination for TOPEX/POSEIDON, *J. Geophys. Res., 99*, 24383-24404, 1994.

Tapley, B. D., M. M. Watkins, J. C. Ries, G. W. Davis, R. J. Eanes, S. Poole, H. J. Rim, B. E. Schutz, C. K. Shum, R. S. Nerem, F. J. Lerch, E. C. Pavlis, S. M. Klosko, N. K. Pavlis, and R. G. Williamson, The JGM-3 Gravity Model, *J. Geophys. Res.*, *101(B12)*, 28029-28049, 1996.

Tralli, D. M., T. H. Dixon, and S. A. Stephens, The Effect of Wet Tropospheric Path Delays on Estimation of Geodetic Baselines in the Gulf of California Using the Global Positioning System, *J. Geophys. Res.*, *93*, 6545-6557, 1988.

Wakker, K. F., Report by the subcommittee on intercomparison and merging of geodetic data, *Rep. LR-638*, Delft Univ. of Technol., May 1990.

Watkins, M. M., Tracking Station Coordinates and Their Temporal Evolution as Determined from Laser Ranging to The Lageos Satellite, Dissertation, Department of Aerospace Engineering and Engineering Mechanics, The University of Texas at Austin, May, 1990.

Wahr, J. M., Body Tides on An Elliptical, Rotating Elastic and Oceanless Earth, *Geophys. J. R. Astron. Soc.*, Vol. 64, 677-703, 1981a.

Wahr, J. M., The forced nutations of an elliptical, rotating, elastic, and oceanless earth, *Geophys. J. R. Astron. Soc.*, Vol. 64, 705-727, 1981b.

Wu, S. C., T. P. Yunck and C. L. Thornton, Reduced-Dynamic Technique for Precise Orbit Determination of Low Earth Satellite*, Proc. AAS/AIAA Astrodynamics Specialist Conference*, Paper AAS 87-410, Kalispell, Montana, August, 1987.

Yuan, D. N., The Determination and Error Assessment of The Earth's Gravity Field Model, Dissertation, Department of Aerospace Engineering and Engineering Mechanics, The University of Texas at Austin, May, 1991.

Yunck, T. P. and S. C. Wu, Non-Dynamic Decimeter Tracking of Earth Satellites Using the Global Positioning System, Paper AIAA-86-0404*, AIAA 24th Aerospace Sciences Meeting*, Reno, Nevada, January, 1986.

Yunck, T. P., W. I. Bertiger, S. C. Wu, Y. E. Bar-Server, E. J. Christensen, B. J. Haines, S. M. Lichten, R. J. Muellerschoen, Y. Vigue, and P. Willis, First Assessment of GPS-based Reduced Dynamic Orbit Determination on TOPEX/Poseidon, *Geophys. Res. Let.*, *21(7)*, 541-544, April 1, 1994.